High-Dimensional Single-Cell Mapping of Central Nervous System Immune Cells Reveals Distinct Myeloid Subsets in Health, Aging, and Disease

Mrdjen, Dunja ; Pavlovic, Anto ; Hartmann, Felix J ; Schreiner, Bettina ; Utz, Sebastian G ; Leung, Brian P ; Lelios, Iva ; Heppner, Frank L ; Kipnis, Jonathan ; Merkler, Doron ; Greter, Melanie ; Becher, Burkhard

DOI: https://doi.org/10.1016/j.immuni.2018.02.014

Resource

Immunity

High-Dimensional Single-Cell Mapping of Central Nervous System Immune Cells Reveals Distinct Myeloid Subsets in Health, Aging, and Disease

Graphical Abstract

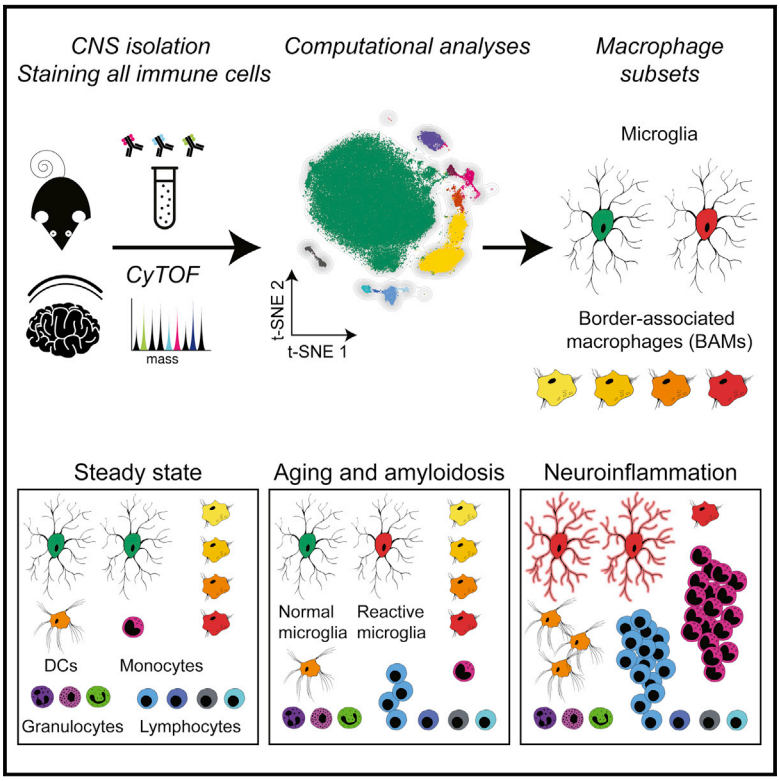

Authors

Dunja Mrdjen, Anto Pavlovic, Felix J. Hartmann, ..., Doron Merkler, Melanie Greter, Burkhard Becher

Correspondence

becher@immunology.uzh.ch

In Brief

It has been challenging to map leukocytes in the brain, particularly during pathology. Mrdjen et al. combine high-dimensional single-cell cytometry with fate mapping to capture the immune landscape of the brain. They identify different subsets of myeloid cells and the phenotypic changes in CNS immune cells during aging and in models of Alzheimer's disease and multiple sclerosis.

Highlights

- High-dimensional cytometry reveals diverse immune cells in the steady-state CNS
- CD38 and MHCII distinguish CNS border-associated macrophage (BAM) subsets
- A subset of microglia responds to aging and neurodegeneration
- All microglia are homogenously affected in neuroinflammatory disease

Mrdjen et al., 2018, Immunity *48*, 380–395
February 20, 2018
https://doi.org/10.1016/j.immuni.2018.01.011

CellPress

CellPress

Immunity
Resource

High-Dimensional Single-Cell Mapping of Central Nervous System Immune Cells Reveals Distinct Myeloid Subsets in Health, Aging, and Disease

Dunja Mrdjen,[1] Anto Pavlovic,[1] Felix J. Hartmann,[1] Bettina Schreiner,[1] Sebastian G. Utz,[1] Brian P. Leung,[1] Iva Lelios,[1] Frank L. Heppner,[2] Jonathan Kipnis,[3] Doron Merkler,[4] Melanie Greter,[1] and Burkhard Becher[1,5,*]

[1]Institute of Experimental Immunology, University of Zurich, Zurich, Switzerland
[2]Department of Neuropathology, Charité-Universitätsmedizin Berlin, Berlin, Germany
[3]Center for Brain Immunology and Glia, Department of Neuroscience, University of Virginia, Charlottesville, VA, USA
[4]Department of Pathology and Immunology, University of Geneva, and Division of Clinical Pathology, Geneva University Hospital, Geneva, Switzerland
[5]Lead Contact
*Correspondence: becher@immunology.uzh.ch
https://doi.org/10.1016/j.immuni.2018.01.011

SUMMARY

Individual reports suggest that the central nervous system (CNS) contains multiple immune cell types with diverse roles in tissue homeostasis, immune defense, and neurological diseases. It has been challenging to map leukocytes across the entire brain, and in particular in pathology, where phenotypic changes and influx of blood-derived cells prevent a clear distinction between reactive leukocyte populations. Here, we applied high-dimensional single-cell mass and fluorescence cytometry, in parallel with genetic fate mapping systems, to identify, locate, and characterize multiple distinct immune populations within the mammalian CNS. Using this approach, we revealed that microglia, several subsets of border-associated macrophages and dendritic cells coexist in the CNS at steady state and exhibit disease-specific transformations in the immune microenvironment during aging and in models of Alzheimer's disease and multiple sclerosis. Together, these data and the described framework provide a resource for the study of disease mechanisms, potential biomarkers, and therapeutic targets in CNS disease.

INTRODUCTION

The central nervous system (CNS) was long regarded as a site of limited immune surveillance due to the lack of obvious lymphatic vessels, the blood brain barrier (BBB), and slow transplant rejection (Murphy and Sturm, 1923; Shirai, 1921). However, the CNS is a compartmentalized organ comprising the parenchyma, the ventricles containing the choroid plexus and cerebrospinal fluid (CSF), the meningeal layers that envelop the parenchyma, and several "absolute" (BBB) and semi-permeable barriers (blood-CSF, blood-leptomeningeal) (Shechter et al., 2013). It is now clear that the level of steady-state immune privilege varies dramatically between compartments.

The parenchyma appears to be the most immune-privileged compartment within the CNS, and in the steady state the only resident leukocytes are microglia: specialized macrophages that are seeded into the brain during embryogenesis (Ginhoux et al., 2010; Schulz et al., 2012), where they contribute to neuronal synapse sculpting and immune surveillance (Colonna and Butovsky, 2017; Prinz and Priller, 2014; Salter and Beggs, 2014). Outside the parenchyma, immune surveillance is mediated by bone-marrow-derived dendritic cells (DCs) (Greter et al., 2005; Kivisäkk et al., 2009) and CNS border-associated macrophages (BAMs), which line the meninges, choroid plexus, and perivascular spaces (Bechmann et al., 2001) and have recently been shown to also be embryonically derived (Goldmann et al., 2016).

During neuro-inflammation, the immune landscape of the CNS changes dramatically; resident immune cells become activated and the parenchyma can be infiltrated by inflammatory leukocytes from the periphery. CNS-resident phagocytes must present cognate self-antigen to encephalitogenic T cells during the course of experimental autoimmune encephalomyelitis (EAE), a murine model of multiple sclerosis (MS) (Schreiner et al., 2009). Several studies assign this role either to DCs or BAMs during the initiation of EAE (Greter et al., 2005; Kivisäkk et al., 2009; Schläger et al., 2016). Also, during aging, inflammation in the brain gradually increases, a process termed "inflammaging" (Deleidi et al., 2015), and CNS leukocytes may also play a role in age-related inflammation and neurodegeneration (Baruch et al., 2013; Prokop et al., 2015; Ritzel et al., 2016).

Despite the importance of CNS-resident leukocytes in these disease processes, our ability to fully characterize these populations and to understand their distinct functions has so far been limited: at present, reliable discrimination of microglia and BAMs (both express low levels of CD45 compared to other leukocytes) can be achieved within tissue sections only by immunohistochemistry methods, where their distinct patterns of localization (parenchyma versus CNS border regions) provide a surrogate for their identification (Goldmann et al., 2016). Moreover, a clear distinction between BAMs and DCs within

cohabited CNS compartments remains challenging. This problem is compounded by the phenotypic changes that occur during various CNS pathologies. For instance, during neuroinflammation, the invasion by peripheral leukocytes makes it virtually impossible to unambiguously discriminate blood-derived leukocytes from tissue-resident populations (Greter et al., 2015).

Here, we describe an approach that overcomes many previous localization- and imaging-dependent limitations to identify and characterize immune cells within the murine CNS. We created a high-dimensional single-cell proteome atlas of immune populations using high parametric mass cytometry (Bandura et al., 2009; Becher et al., 2014) combined with location information from immunohistochemistry (IHC) and verified by 22-color fluorescence cytometry and reporter and fate-mapping systems. We uncovered the existence of cellular subsets within CNS-resident phagocyte populations at steady state and further defined the entire immune landscape during aging, neurodegeneration, and neuroinflammation, highlighting the differences and similarities between these different forms of CNS pathology. This comprehensive immune cell atlas of the mammalian CNS will enable the study of individual leukocyte populations and their roles in CNS development, homeostasis, and disease.

RESULTS

The Steady-State CNS Contains Diverse Resident Immune Cell Populations

We employed an integrated set of strategies to enable mapping of the immune cell populations within the murine CNS, as shown in Figure 1A. To capture the complexity of cellular phenotypes, we designed a 43-heavy metal isotope-tagged surface antibody panel for mass cytometry (Table S1). Mass cytometry data were further complemented by 22-color fluorescence cytometry, and the location of specific cell populations within the CNS was analyzed by IHC.

We first interrogated the steady-state CNS in 8-week-old C57BL/6 mice. To give an overview of all immune populations present, mass cytometry data was visualized in a t-SNE map and cells categorized by FlowSOM-guided clustering (Figures 1B, 1C, and S1A; Hartmann et al., 2016). This approach revealed a substantial amount of complexity of leukocytes within the normal CNS: microglia and other macrophage-like cells, several types of monocytes (Ly6C^{hi} and Ly6C^{lo} monocytes and monocyte-derived cells [MdCs]), as well as classical DCs (cDCs), plasmacytoid DCs (pDCs), B cells (CD24^{+} and CD24^{-}, see Figure S1A), T cells, natural killer (NK) cells, NKT cells, innate lymphoid cells (ILCs), eosinophils, and mast cells. Traditional manual gating of the mass cytometry data confirmed the identity of these cell populations (Figure S1B). Microglia (CD45^{lo}CD11b^{lo}F4/80^{+}CD64^{+}MeTK^{+}Cx3CR1^{hi}Siglec-H^{+}CD88^{lo}) were the most abundant immune cells in the steady-state CNS (Figure 1D). We were also able to identify a separate population of cells with a closely related surface protein expression pattern (CD45$^{lo/+}$CD11b^{lo}F4/80^{hi}CD64^{hi}MeTK^{+}Cx3CR1^{+}CD88^{hi}); however, these cells lacked typical microglial Siglec-H expression and instead expressed CD206 and CD38 (Figures 1C and S1A).

Using IHC, Goldmann et al. (2016) recently described a population of embryonically derived macrophages with a microglia-like phenotype that occupy distinct locations, namely the border regions of the CNS in contrast to the parenchyma where only microglia reside. We hypothesized that the non-microglia macrophage-like cells identified in our unbiased analysis were in fact BAMs. These BAMs are virtually indistinguishable from microglia using conventional (CD45 versus CD11b) gating strategies (Figure S1B).

To confirm this and the identities of the other cell populations present, we first used functional assays that exploit characteristic cell type-restricted responses to different stimuli. We treated mice with either an antagonistic colony-stimulating factor 1 receptor) (CSF1R) antibody to deplete tissue-resident macrophages and Ly6C^{lo} monocytes, but not microglia (which are likely protected by the BBB) or Ly6C^{hi} monocytes (Hoeffel et al., 2015), or with the recombinant growth factor Flt3L, which specifically expands DCs (Maraskovsky et al., 1996; Anandasabapathy et al., 2011). Indeed, anti-CSF1R treatment depleted the cells we identified as BAMs and Ly6C^{lo} monocytes but had no effect on other cell types (Figure 1E). The depletion of BAMs further confirms their location within the border regions of the CNS where the vasculature has different barrier properties to the BBB of the parenchymal vasculature (Engelhardt et al., 2017). Flt3L treatment in turn increased the frequency of DCs, as well as Ly6C^{hi} monocytes and MdCs (after 9 days of treatment, the bone-marrow monocyte progenitors are also targeted), while having no effect on microglial, BAM, or Ly6C^{lo} monocyte populations (Figure 1E), thus functionally confirming our algorithm-guided population identification.

To determine whether the leukocytes we detected in the CNS were within the tissue itself or within the lumen of vessels or capillaries, we intravenously injected fluorescently (PE)-labeled anti-CD45 antibodies (Anderson et al., 2014). More than 98% of control blood leukocytes were labeled with anti-CD45-PE, while only 5% of CNS leukocytes were labeled (Figures S2A–S2C); thus 95% of all CNS leukocytes identified are *bona fide* extra-vascular CNS-resident cells. Neutrophils constituted the third largest leukocyte population in the CNS, 81.8% ± 3.0% being unlabeled and therefore tissue resident (Figures S2D and S2E). Tissue sections revealed neutrophils predominantly within the dura mater (Figure S2F), as well as the pia mater and the ependyma (data not shown) of the steady-state CNS. Together, our analysis of the steady-state CNS revealed multiple immune cell populations residing within CNS compartments, including a subset of microglia-like BAMs.

BAMs Are CNS-Resident Macrophages that Are Distinct from Microglia

We used our mass cytometry data to design a 22-color antibody panel for fluorescence cytometry (Table S1) that identified all the major leukocytes in the CNS. This allowed us to use genetic reporter and fate-mapping experiments aimed at determining the relationship between BAMs, microglia, and CNS DCs. To compare the mass and fluorescence cytometry datasets and their ability to identify the same cell populations, we employed force-directed analysis to generate a Scaffold map (Spitzer et al., 2015): we first modeled a reference map of CNS leukocytes from our mass cytometry data, using manually gated populations as landmark nodes (in colors) and the initial 100 FlowSOM nodes (before metaclustering) as unsupervised nodes (in gray) (Figure 2A). Mapping the flow cytometry data onto this mass cytometry-based

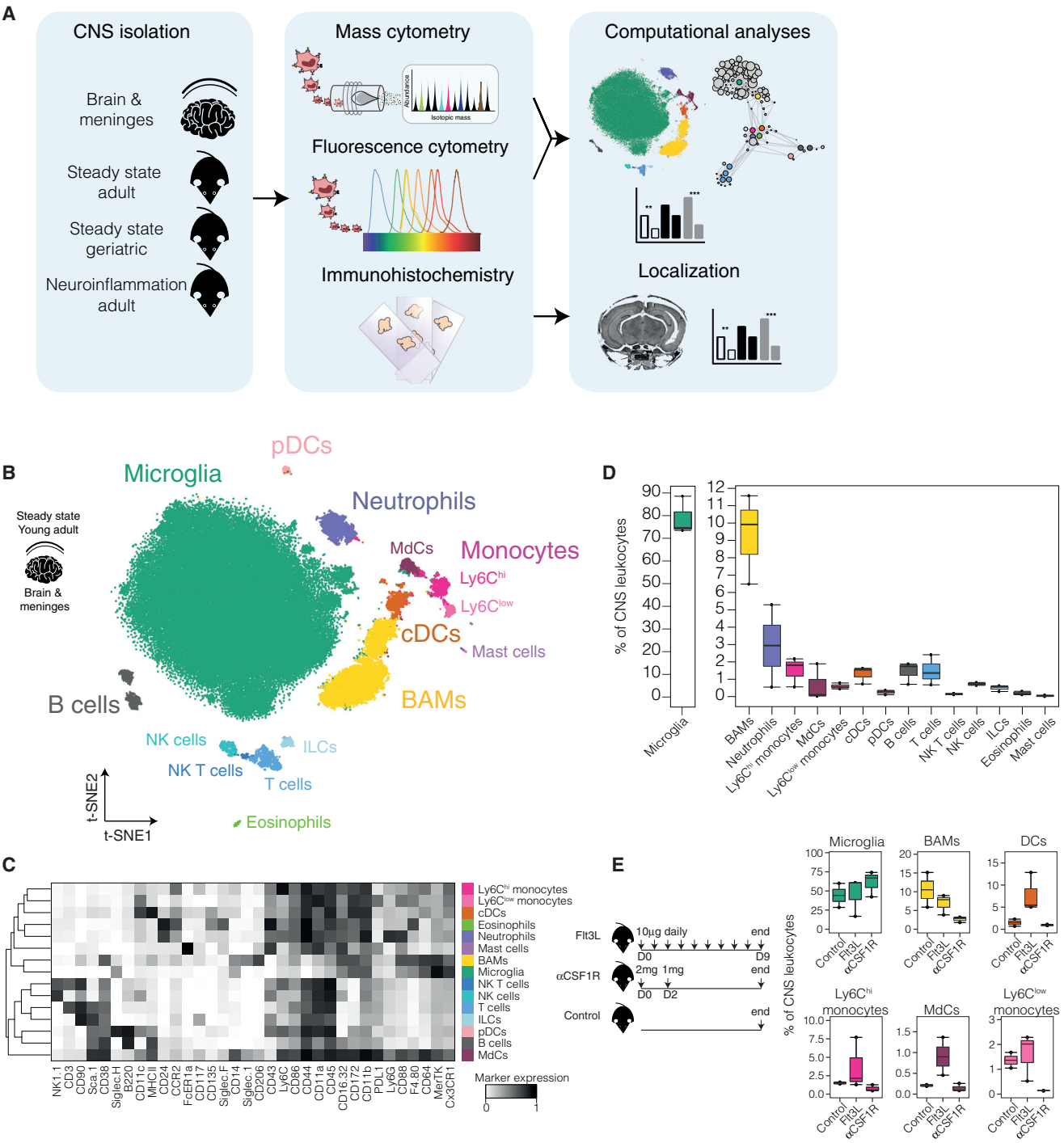

Figure 1. Mass Cytometry Identifies CNS-Associated Leukocyte Diversity in the Steady-State

Figure360▷ For a Figure360 author presentation of Figure 1, see the figure legend at http://dx.doi.org/10.1016/j.immuni.2018.01.011.

(A) Schematic representation of the experimental approach.

(B) t-SNE map displaying 100,000 randomly sampled cells from the CNS of steady-state 2-month-old C57BL/6 mice analyzed by mass cytometry. Colors correspond to FlowSOM-guided clustering of cell populations (n = 3, representative of 6 independent experiments).

(C) Median marker expression values for each population.

(D) Frequencies of steady-state CNS leukocytes.

(E) Experimental schematic (left) and frequencies (right) of myeloid populations within total CNS leukocytes after indicated treatments (n = 3).

See also Figures S1 and S2 and Table S1. Error bars represent range.

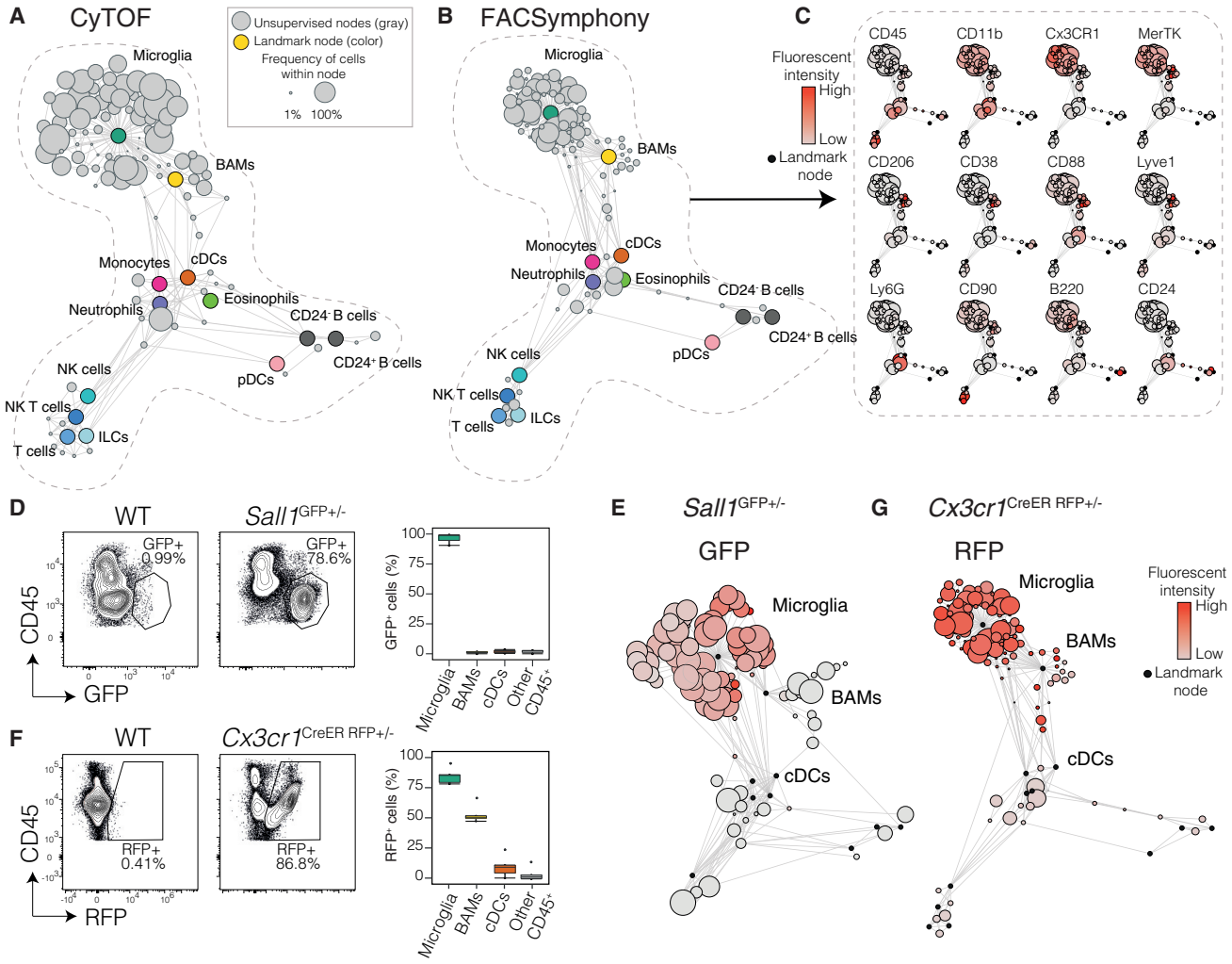

Figure 2. Microglia and BAMs Are Distinguished by Genetic Targeting

(A) A Scaffold reference map of the steady-state adult CNS leukocyte landscape constructed from mass cytometry data displaying 100 unsupervised FlowSOM nodes and manually gated landmark nodes.

(B) Fluorescence cytometry data of steady-state adult CNS leukocytes mapped onto the reference map created in (A).

(C) Representative fluorescent marker expression in the Scaffold map.

(D) CD45$^+$ CNS leukocytes (left) and frequency of GFP$^+$ cells (right) in *Sall1*$^{GFP+/-}$ reporter mice (n = 3, representative of two independent experiments).

(E) GFP expression overlaid onto the *Sall1*$^{GFP+/-}$ Scaffold map.

(F) CD45$^+$ CNS leukocytes (left) and frequency of RFP$^+$ cells (right) in *Cx3cr1*^{CreER} *Rosa26*-RFP mice 5 weeks after tamoxifen treatment. (n = 5, showing 4 pooled experiments).

(G) RFP expression overlaid onto the *Cx3cr1*^{CreER} *Rosa26*-RFP Scaffold map.

See also Figure S3. Error bars represent range.

reference map showed that cells within unsupervised nodes that grouped around the landmark nodes had the expected expression profiles and were present at similar frequencies to those in the original reference map (Figures 2B and 2C).

We then examined cells from the CNS of *Sall1*^{GFP} reporter mice. Sall1 is a transcription factor expressed by microglia in adult mice, and in *Sall1*^{GFP} mice the green fluorescent protein (GFP) is produced along with real-time expression of Sall1 (Buttgereit et al., 2016). We found that GFP expression in *Sall1*^{GFP} mice was exclusive to microglia, and Sall1 did not label BAMs or cDCs (Figures 2D and 2E and as a clustered t-SNE in Figure S3A). Thus, in addition to the phenotypic distinctions between BAMs and microglia revealed by mass cytometry, we confirmed Sall1 as a key transcription factor, which can be used to distinguish these closely related cell populations and further confirmed that our cluster assignment of microglia and BAMs as separate populations was correct.

Microglia and the majority of BAMs are long lived (Goldmann et al., 2016) while DCs are bone-marrow derived and short lived (Merad and Manz, 2009). To utilize this difference in longevity for the identification of myeloid cell populations within the CNS, we used *Cx3cr1*^{CreER} *Rosa26*-RFP inducible fate-map mice where tamoxifen induces irreversible expression of red fluorescent protein (RFP) in CX3CR1$^+$ cells (Yona et al., 2013). Short-lived

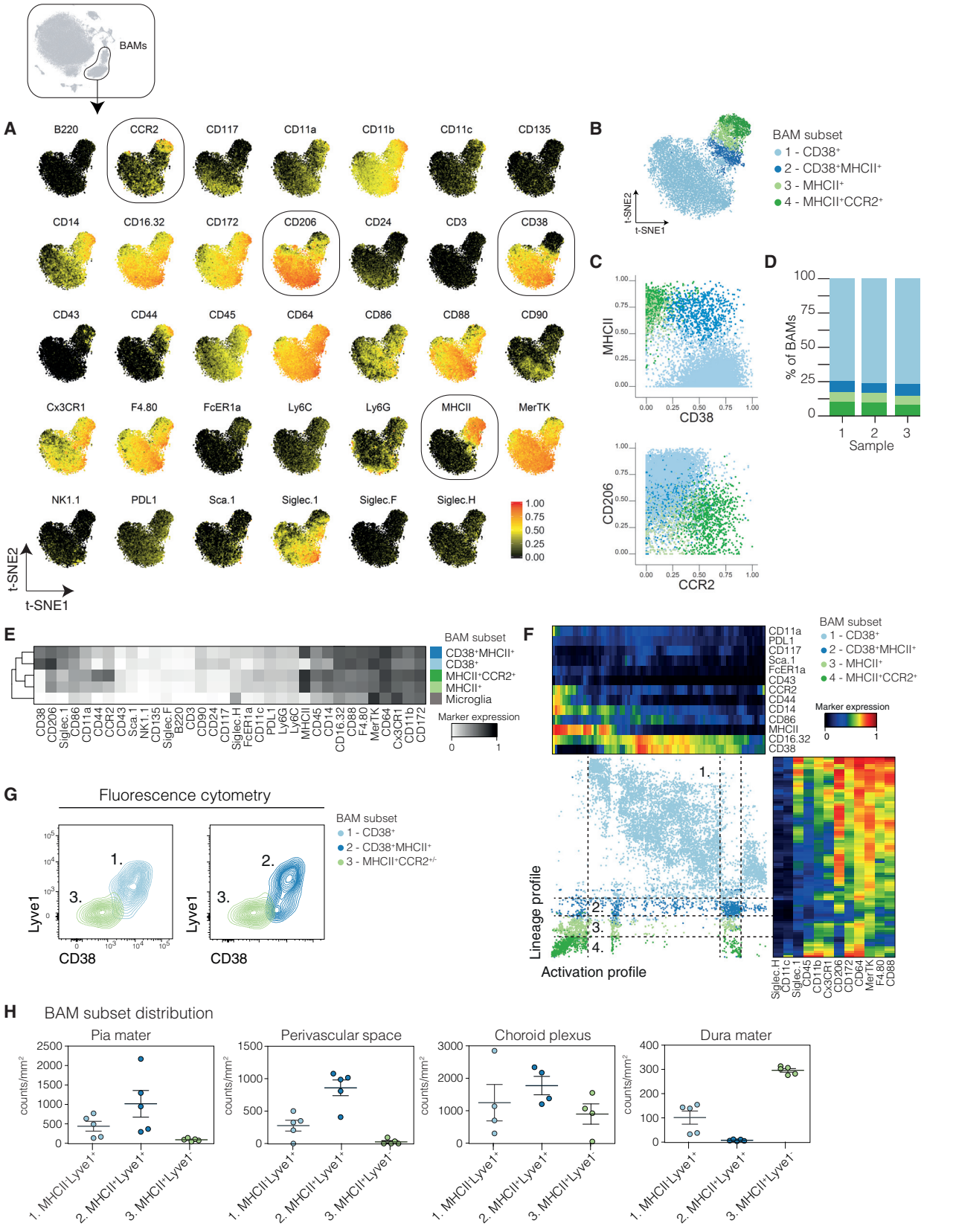

(legend on next page)

labeled cells will be replaced from unlabeled bone marrow progenitors, while long-lived or self-renewing cells will remain RFP$^+$. Here, 5 weeks after tamoxifen treatment of adult *Cx3cr1*^{CreER} *Rosa26*-RFP mice, less than 5% of monocytes were RFP$^+$ (Figure S3B), while almost 80% of microglia, 50% of BAMs, and less than 10% of DCs were RFP$^+$ (Figures 2F and 2G). Most BAMs retained the RFP label, as a result of the earlier tamoxifen treatment, whereas most DCs lost RFP expression. Hence, we concluded that CX3CR1$^+$ BAMs are replaced more slowly than CX3CR1$^+$ DCs. This differential longevity combined with the lack of Sall1 expression by non-microglial cells confirms that the high-dimensional map produced here corresponds to the predicted ontogeny of CNS leukocytes.

Specific BAM Subsets Are Enriched in Distinct CNS Compartments

Now that we could reliably discriminate BAMs from microglia and DCs, we conducted an in-depth BAM phenotype analysis. This revealed expression of the macrophage-associated markers MerTK, CD64, and F4/80, as well as CD16/32 (Figure 3A), and absence of the DC, monocyte, and microglia markers CD11c, Ly6C, and Siglec-H, respectively. Further, we identified four BAM subsets based on differential expression of CD38, MHCII, and CCR2: subset 1 (CD38$^+$MHCII$^-$CCR2$^-$), subset 2 (CD38$^+$MHCII$^+$CCR2$^-$), subset 3 (CD38$^-$MHCII$^+$CCR2$^-$), and subset 4 (CD38$^-$MHCII$^+$CCR2$^+$) (Figures 3B and 3C). The median expression values of each marker in the different BAM subsets are compared in a heatmap (Figure 3D). The majority of BAMs (75.7% ± 1.2%) were situated within subset 1, while subsets 2, 3, and 4 comprised 7.6% ± 0.8%, 7.2% ± 0.2%, and 9.4% ± 1.2% of total BAMs, respectively (Figure 3E). Subsets 3 and 4 were almost identical but differed in the amount of CCR2, CD44, and CD206. To understand the full heterogeneity and distinct high-dimensional phenotypes of the four BAM subsets at the single-cell level, we employed categorical One-SENSE analysis (Cheng et al., 2016), where the y axis represents the lineage profile, the x axis represents an activation marker profile (Figure 3F), and co-regulation of marker expression is also shown, e.g., CD206 expression was high on subset 1 but decreased as the activation markers MHCII and CD44 increased toward subsets 2, 3, and 4 while high expression of other macrophage markers like CD64 was maintained.

We then used confocal microscopy to ask whether these subsets are enriched in specific compartments of the CNS. The available anti-mouse CD38 performed poorly in IHC, but using fluorescence cytometry we found that Lyve1 and CD38 expression closely overlapped (Figures 3G and S4A) and therefore that Lyve1 was a suitable surrogate for CD38 on BAMs. As lymphatic vessels also express Lyve1 and are present in the dura mater (Louveau et al., 2015), we also stained for collagen IV, which is expressed on vessels but not BAMs. Combining Lyve1 or MHCII with the macrophage marker Iba-1, we located BAMs within the pia mater, perivascular space, choroid plexus, and dura mater and showed that they express CD206, as previously shown (Figure S4B; Goldmann et al., 2016). By histology, we identified three BAM subsets in these regions using differential Lyve1 and MHCII expression (Figure S4C). The initial CyTOF-identified subsets 3 and 4 are merged here. Of note, Lyve1$^+$MHCII$^+$ (subset 2) BAMs were enriched in the pia mater and perivascular space, whereas the dura mater harbored relatively more single-positive MHCII$^+$ BAMs (subsets 3 and 4) and few Lyve1$^+$MHCII$^+$ BAMs (Figure 3H). The choroid plexus contained a similar frequency of each of the three BAM subsets. Single-positive Lyve1$^+$ BAMs (subset 1) were present in all locations. Only MHCII$^+$ BAMs, enriched in the choroid plexus and dura mater, expressed CCR2$^+$ (Figure 3B) (subset 4), consistent with their proposed high turnover rate and replacement by CCR2$^+$ bone marrow-derived cells within the choroid plexus (Goldmann et al., 2016). Together, these data showed that BAMs are heterogeneous macrophages that can be divided into subsets based on their distinct expression of CD38 and MHCII and are specifically enriched in different CNS compartments. The phenotypic variations of BAMs across the CNS may reflect functional differences and could be shaped by cues from their specific local microenvironments.

Heterogeneous Subsets of DCs Exist in the CNS

In addition to BAMs, DCs also localize in the CNS border regions and are considered to be the prime antigen-presenting cells (APCs) at these sites (Anandasabapathy et al., 2011; Greter et al., 2005). In other tissues, DCs exist as functionally and phenotypically distinct subsets but little is known of the DCs associated with the CNS. We used our mass cytometry datasets to perform an in-depth phenotypic characterization of CNS-associated DCs (Figure 4A). We identified three main DC subsets corresponding to cDC1s, cDC2s, and pDCs (Figure 4B), differentiated by their expression of CD11b (or CD172) and CD24 (Figure 4C). In addition, Ly6C, B220, or Siglec-H confirmed the pDC identity of subset 6. The cDC2 population was heterogeneous and could be further separated into CD24$^+$CD206$^+$ cDC2 (subset 1), CD24$^-$CD64$^{+/lo}$CD206$^{-/lo}$ cDC2 (subset 2), CD135^{hi} cDC2 (subset 3), and PDL1$^+$ cDC2 (subset 4), while cDC1s (subset 5) were CD11b^{lo}CD172^{lo}CD24$^+$CD135^{hi}CD117$^+$ (Figure 4D). As in most other organs (Guilliams et al., 2016), cDC2s were relatively more abundant than cDC1s (Figure 4E). The lineage markers and activation profiles of these subsets were again fully revealed using categorical One-SENE (Figure 4F). We localized

Figure 3. BAMs Exist as Phenotypically Distinct Subsets Enriched in Specific CNS Compartments

(A) CNS BAMs were plotted onto a separate t-SNE. Outlined plots represent four distinguishing markers of BAM subsets.
(B) BAMs clustered into four subsets based on the entire panel of markers.
(C) Expression of CD38, MHCII, CCR2, and CD206 by the four BAM subsets (colored).
(D) Relative frequencies of the four BAM subsets across 3 mice (n = 3, representative of 4 independent experiments).
(E) Median expression of mass cytometry markers on each BAM subset and microglia.
(F) One-SENSE analysis of BAMs along lineage and activation profiles.
(G) Fluorescence cytometry data depicting expression of Lyve1, CD38, and MHCII in three BAM subsets.
(H) Density of BAM subset occurrence within each region of interest (ROI) (n ≥ 5 mice, ROI ≥ 4 per mouse).
See also Figure S4. Error bars represent the median ± SEM.

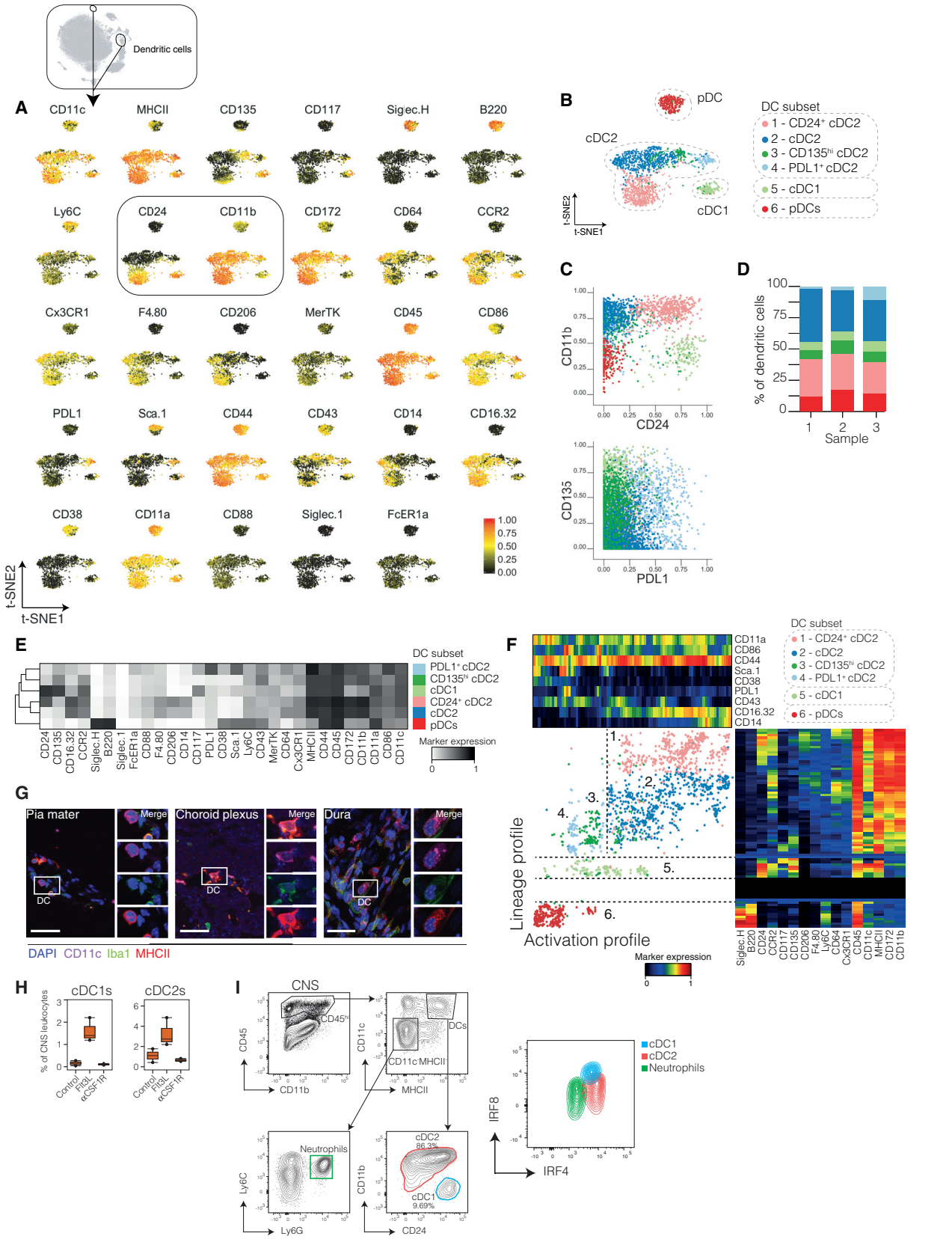

(legend on next page)

$CD11c^+MHCII^+$ DCs of the CNS by confocal microscopy only in the choroid plexus, pia mater, and dura mater, and not in the perivascular space (Figure 4G), suggesting that these DC-enriched compartments may serve as entry sites for MHC-dependent T cells.

As we have shown that CNS cDC2s exist with some heterogeneity in their surface phenotype, we sought to confirm their inherent identity compared to cDC1s. Both cDC2s and cDC1s expanded to a similar extent with Flt3L treatment (Figure 4H) and moreover cDC1s were $IRF8^{hi}IRF4^{int}$ and cDC2s were $IRF8^{-}IRF4^{hi}$ (Figure 4I), as previously predicted (Guilliams et al., 2016). The apparent heterogeneity of cDC2s has also been noted at other organs such as the lung (Schlitzer et al., 2013) and heart (Clemente-Casares et al., 2017). Thus, our mass cytometry analysis of CNS-associated DCs revealed the presence of the three main DC subsets also represented in other organs of the body. This strengthens the notion that also in the CNS, DCs are the prime APCs among all resident leukocytes and vital for the homeostatic immune surveillance of the CNS.

Aging and Neurodegenerative Disease Change the CNS Immune Cell Landscape

Aging has profound effects on the entire CNS landscape. We therefore asked how the immune cell populations in the CNS changed in aged mice by comparing geriatric mice aged 1.5 years with younger adult mice aged 2 months. We first noted a substantial increase in the frequency of T cells from 1.5% ± 0.9% in adult mice to 11.1% ± 4.2% in geriatric mice, while NKT cells and pDCs were significantly less frequent in geriatric mice ($p = 0.028$ and 0.029, respectively) (Figures 5A and 5B). We also observed an increased frequency of $CD38^+MHCII^+CCR2^-$ and $CD38^-MHCII^+CCR2^-$ BAMs and a corresponding decrease in $CD38^+MHCII^-CCR2^-$ and $CD38^-MHCII^+CCR2^+$ BAMs in geriatric mice (Figure 5C); alongside, the frequency of $CD24^+$ cDC2s decreased, while $CD135^+$ cDC2s were more abundant in geriatric mice (Figure 5D).

We found a phenotypic signature in a subset of microglia in geriatric mice which expressed high levels of CD11c and CD14 (Figure 5E). Aging is a major risk factor for neurodegenerative diseases, and changes in microglial morphology precede pathology in Alzheimer's patients (Perry and Holmes, 2014; Streit et al., 2009). We therefore asked whether the age-related changes in leukocyte populations and the age-associated microglial phenotype in particular were present in a murine model of Alzheimer's disease (AD). We compared the plaque-harboring cortex with the non-plaque-harboring cerebellum (internal control) of 4-month-old APP/PS1 mice (Radde et al., 2006; Vom Berg et al., 2012), and age-matched WT littermates (external control). We found that, as in much older geriatric mice, the frequency of T cells was increased in the plaque-harboring cortex of AD-prone mice (Figure S3A); while, in contrast to geriatric mice, the subset distribution of BAMs was unaltered in AD-prone mice (Figure S3B), suggesting it to be a phenomenon observed during normal aging.

We also detected a phenotypic signature in a subset of microglia in AD-prone mice that resembled microglia in geriatric mice in the expression of CD11c and CD14 (among other markers, data not shown), and which was absent in WT littermate controls (Figure 5F). Approximately 11.9% ± 6.5% of microglia had this signature in geriatric mice, compared to virtually zero in young adult mice, and approximately 13.2% ± 1.7% in the plaque-bearing cortex of AD-prone mice, while these cells were almost undetectable in the unaffected cerebellum and in WT littermate cortex or cerebellum (Figures 5G and S3C). A similar subset of microglia was also described by Keren-Shaul et al. (2017) by sc-RNaseq in 5XFAD mice. We located these $CD11c^+$ microglia around Aβ plaques in APP/PS1 mice (Figure S3D). The full signature of these reactive microglia compared to non-reactive microglia in geriatric mice (fold change) shows that, in addition to increased phagocytosis-associated markers CD11c and CD14, there was an accompanying increase in activation markers CD86 and CD44 and the inhibitory ligand PDL1 (Figure 5H). MHCII expression increased slightly while expression of microglial homeostatic checkpoint markers CX3CR1, MerTK, and Siglec-H decreased. This phenotypic change within the small age- and AD-associated subset represents a switch from a homeostatic microglial program to a "reactive" signature that displays an activated, phagocytic profile (Hanisch and Kettenmann, 2007; Krasemann et al., 2017).

Autoimmune-Neuroinflammation Results in Leukocyte Invasion and Global Changes in the CNS Immune Landscape

We induced EAE in adult C57BL/6 mice and compared the immune cellular composition of the CNS at the peak of disease with steady-state control mice (Figures 6A and S6A). Analyzing the frequencies (Figures 6B and S6C) and cell numbers (Figure S6C) of CNS leukocytes, we found that the majority of infiltrating cells were MdCs, followed by T cells.

Microglia were highly reactive during EAE and exhibited a markedly different phenotypic signature than in the steady state, as evidenced by their change in localization on the t-SNE map (Figure 6A). The microglial identity of these highly reactive cells during EAE was confirmed in *Sall1*^{GFP} reporter mice (Figures 6C and S6D). We then conducted an in-depth analysis of the phenotypic changes in microglia in response to EAE

Figure 4. Dendritic Cells in the Steady-State CNS Exist as Three Main Subsets

(A) CNS DCs were plotted onto a separate t-SNE. Selected plots represent four chosen distinguishing markers.
(B) DCs clustered into three major subsets based on the entire panel of markers.
(C) Expression of distinguishing markers by the DC subsets.
(D) Relative abundance of the DC subsets within total CNS DCs across 3 mice (n = 3, representative of at least 3 experiments).
(E) Median expression of mass cytometry panel markers on each DC subset.
(F) One-SENSE analysis of DCs by their lineage and activation profiles.
(G) Representative fluorescence immunohistochemistry images of DCs in the pia mater, choroid plexus, and dura mater (n ≥ 2 mice, ≥ 3 sections per mouse).
(H) cDC1 and cDC2 response to the indicated stimuli.
(I) IRF4 and IRF8 expression by cDC1s and cDC2s.
Error bars represent range.

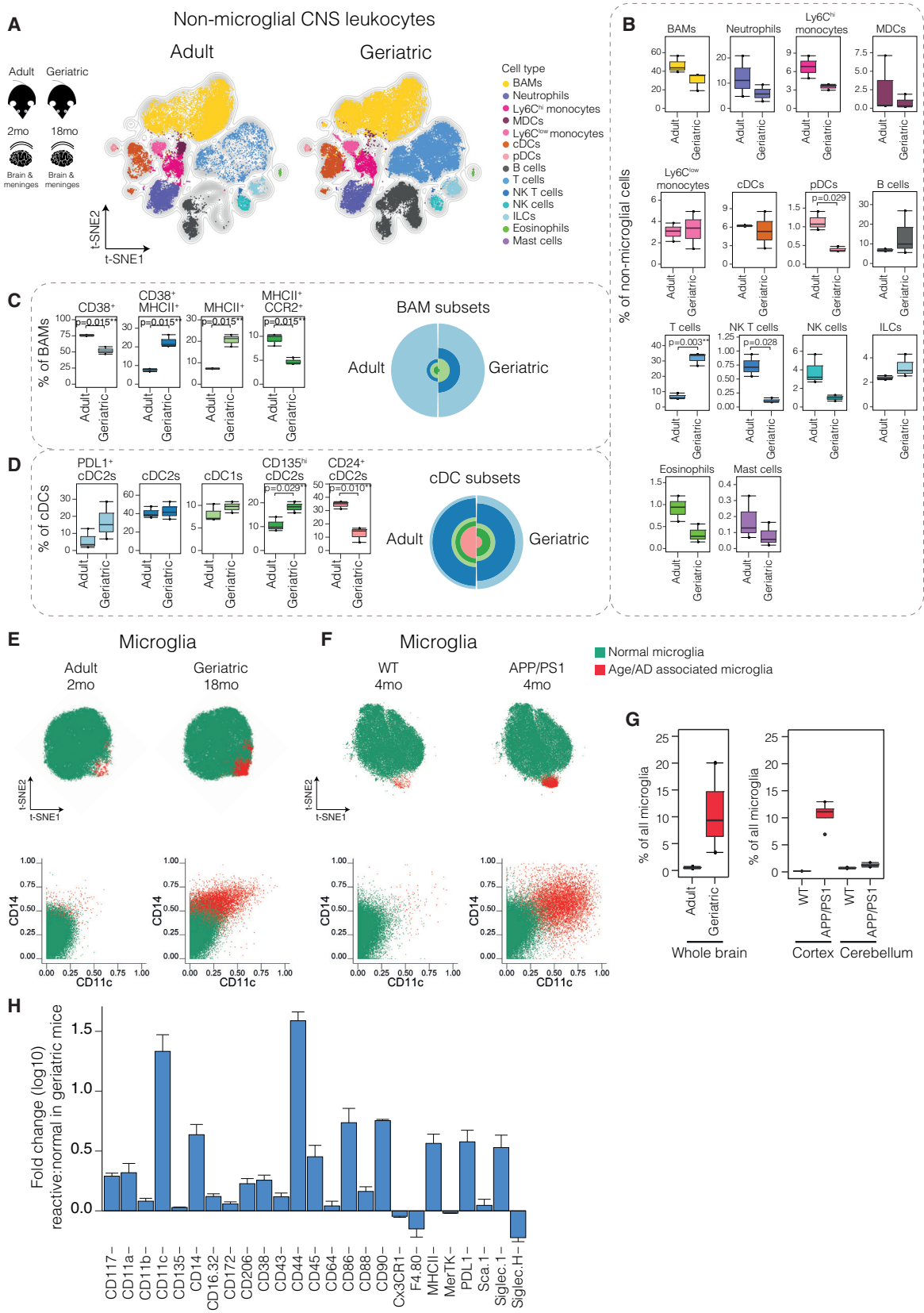

(legend on next page)

inflammation: once again, expression of microglial homeostatic checkpoint markers CX3CR1, MerTK, and Siglec-H was reduced, and expression of markers CD44, CD86, PDL1, and CD11c increased, as similarly observed in geriatric mice. However, in contrast to age- and AD-associated microglia, CD14 expression decreased during EAE and an increase in MHCII and Sca-1 was observed (Figures 6D, 6E, and S6E). The conversion from the homeostatic microglial signature to a highly reactive state signature was also evident when comparing lineage and activation profiles using categorical One-SENSE (Figure 6F). Here and in the t-SNE map (Figures 6A and S6E), there are very few EAE microglia that are located in the same area as steady-state microglia. This is because of a shift in both the lineage and activation profiles of the entire microglia population. Of note, this phenotypic change affects the entire microglial population homogeneously, which is in stark contrast to the small subset of reactive microglia in aging and neurodegenerative disease.

BAMs, MdCs, and DCs share a number of lineage markers. Interrogating their profiles more closely in EAE, we found that MdCs, monocytes, and cDCs were more similar to each other while BAMs and pDCs were distinctly separated on the t-SNE map (Figure S7A). We used *Cx3cr1*^{CreER} *Rosa26*-RFP EAE mice to validate that BAMs and MdCs were indeed identified correctly. At peak EAE, as in steady state, only microglia and BAMs were RFP^{+} (Figures 7A and S7B). However, the number of total and RFP^{+} BAMs decreased during EAE relative to steady state and BAMs became outnumbered by infiltrating MdCs (Figures 7B and S6C). As with microglia, the phenotype of all BAMs was altered in EAE (Figure 7C): inflammation led to increased expression of MHCII and the activation markers CD44 and Sca-1, as well as PDL1, CD117, and CD11c (Figure 7D).

Ly6C^{hi} monocytes invade the CNS parenchyma and differentiate into inflammatory and pathogenic MdCs during EAE (Codarri et al., 2013; Croxford et al., 2015a, 2015b; Yamasaki et al., 2014). This differentiation program is supported by our data as Ly6C^{hi} monocytes did not yet undergo inflammation-induced phenotypic changes (Figure S7A), while MdCs were highly activated, expressing Sca-1, MHCII, PDL1, CD11a, CD86, CD38, CD14, and CD16/32 and a macrophage-like lineage profile (Figure 7E). This profile has previously rendered them hard to distinguish from microglia and BAMs. We also distinguished cDC subsets and pDCs and show their lineage and activation profiles during peak EAE (Figure 7F).

Finally, we defined a myeloid panel of 12 markers within our mass cytometry data to clearly discern reactive microglia, BAMs, MdCs, and cDCs even in the inflamed CNS (Figure 7G). Together, our analysis shows that CNS-resident myeloid cells become highly activated during neuroinflammation but can still be distinguished from macrophage-like invading MdCs, confirming the utility of our high-dimensional myeloid immune atlas as a valuable resource for marker combinations allowing mapping of cellular subsets in downstream analyses.

DISCUSSION

We have systematically characterized the leukocyte landscape within the mammalian CNS under a range of conditions. While lymphocyte populations can be readily identified via expression of unique canonical antigens, and recent reports have begun to characterize them in the steady-state CNS (Korin et al., 2017), CNS myeloid cells have proven highly challenging to study. The CNS myeloid compartment is the largest CNS-resident immune cell population and has been implicated in multiple aspects of CNS health and disease, including MS, AD, dementia, and Parkinson's disease, as well as psychiatric diseases and behavioral disorders like schizophrenia, autism, and depression (Herz et al., 2017; Kettenmann et al., 2013; Prinz and Priller, 2014). Using high-dimensional cytometry in combination with neural-network based algorithms, we identified microglia, BAMs, DCs, and monocytes as separate populations by extensive surface protein phenotyping. These data were corroborated by functional, genetic, and fate-mapping approaches.

Interrogating these cells in the high-dimensional space led us to uncover four previously uncharacterized BAM subsets, distinguished by differential expression of CD38 or Lyve1, MHCII, and CCR2. It is likely that the CCR2^{+} subset (subset 4) represents a fresh hematopoietic myeloid cell to replace the BAMs that accumulate in the choroid plexus (Goldmann et al., 2016) and dura mater. We showed that single-positive CD38^{+} or Lyve1^{+} BAMs made up approximately 30% of pial BAMs and that they can be CX3CR1$^{lo/-}$. Thus this BAM subset may not be efficiently targeted by the commonly used *Cx3CR1*^{CreER} *Rosa26* fate-map system. On the other hand, MHCII^{+} BAM subsets expressed high levels of CX3CR1 and were therefore likely targeted better in this system. The dura mater distinctly lacked Lyve1^{+}MHCII^{+} BAMs, but these BAMs were enriched in the pia mater, perivascular space, and choroid plexus. The dura mater harbored predominantly Lyve1^{-}MHCII^{+} BAMs. The function of the phenotypically different dural BAMs in CNS homeostasis and disease likely differs from pial, perivascular, and choroid plexus BAMs as the dura is not in physical contact with the brain and encloses a lymphatic system (Aspelund et al., 2015; Louveau et al., 2015). With our surface protein profile of BAMs, it is now possible to purify their subsets for detailed study into their potential roles in, e.g., vascular maintenance, immune suppression, or activation.

Figure 5. Aging Causes an Altered CNS Immune Landscape and a Subset of Reactive Microglia Emerges

(A) Non-microglial CNS leukocytes from adult (2-month-old) and geriatric (1.5-year-old) C57BL/6 mice analyzed by mass cytometry.

(B–D) Frequencies of (B) non-microglial CNS leukocytes, (C) BAM, and (D) cDC subset distributions in adult and geriatric mice.

(E) Normal and reactive microglia differentiated by CD14 and CD11c expression in adult and geriatric mice (n = 3).

(F) Normal and reactive microglia in 4-month-old WT and APP/PS1 mice (n = 2–4, experiment repeated twice).

(G) Frequencies of age- or AD-associated microglia in adult versus geriatric C57BL/6 mice, or the cortex (plaque-harboring) and cerebellum (internal control) of WT versus APP/PS1 mice, respectively.

(H) Fold change (log10) in expression of myeloid markers in the mass cytometry panel between normal and reactive microglia in geriatric mice.

**p value significant (< 0.05) with a Benjamini-Hochberg (BH) false discovery rate (FDR) < 5%. Error bars represent range except in (H) where error bars represent the median ± SEM. See also Figure S5.

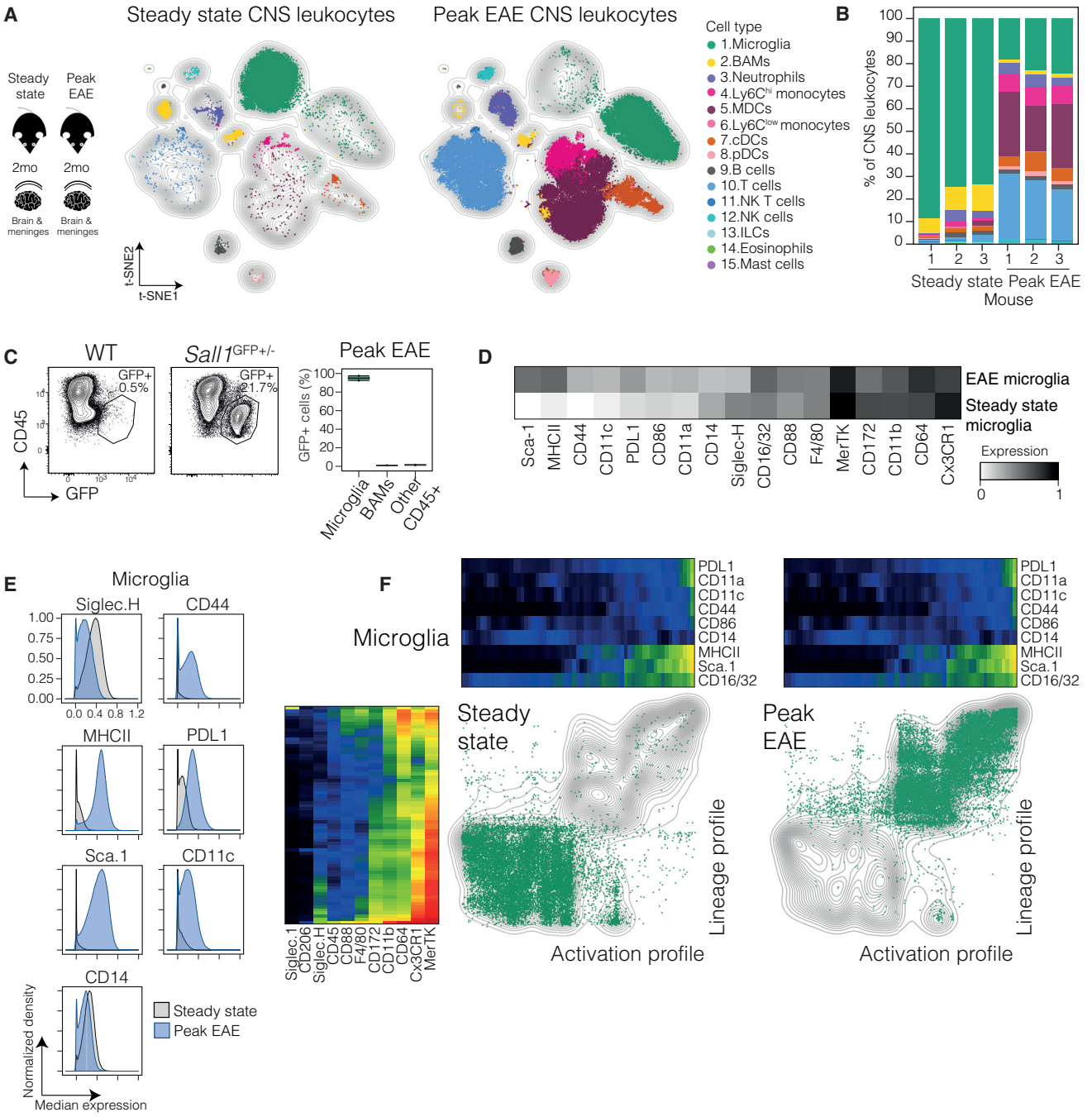

Figure 6. Neuroinflammation Is Accompanied by CNS Invasion and Homogeneous Microglial Activation

EAE was induced in adult (2-month-old) C57BL/6 mice and CNS cells were analyzed by mass cytometry at the peak of disease and in control steady-state mice.

(A) Clustered leukocytes on a t-SNE map generated from the combined steady-state and EAE data (100,000 cells).

(B) Frequencies of leukocytes within total CNS leukocytes in steady-state and peak EAE (n = 3, representative of 5 independent experiments).

(C) CD45$^+$ CNS leukocytes (left) from *Sall1*$^{GFP+/-}$ reporter and control mice at peak EAE, with quantification (right) of GFP$^+$ cells (n = 3, representative of two independent experiments).

(D) Median expression profiles of steady-state and peak EAE microglia.

(E) Representative histograms showing highly upregulated makers between steady-state and peak EAE microglia.

(F) One-SENSE analysis comparing the lineage and activation profiles of steady-state and peak EAE microglia.

See also Figure S6.

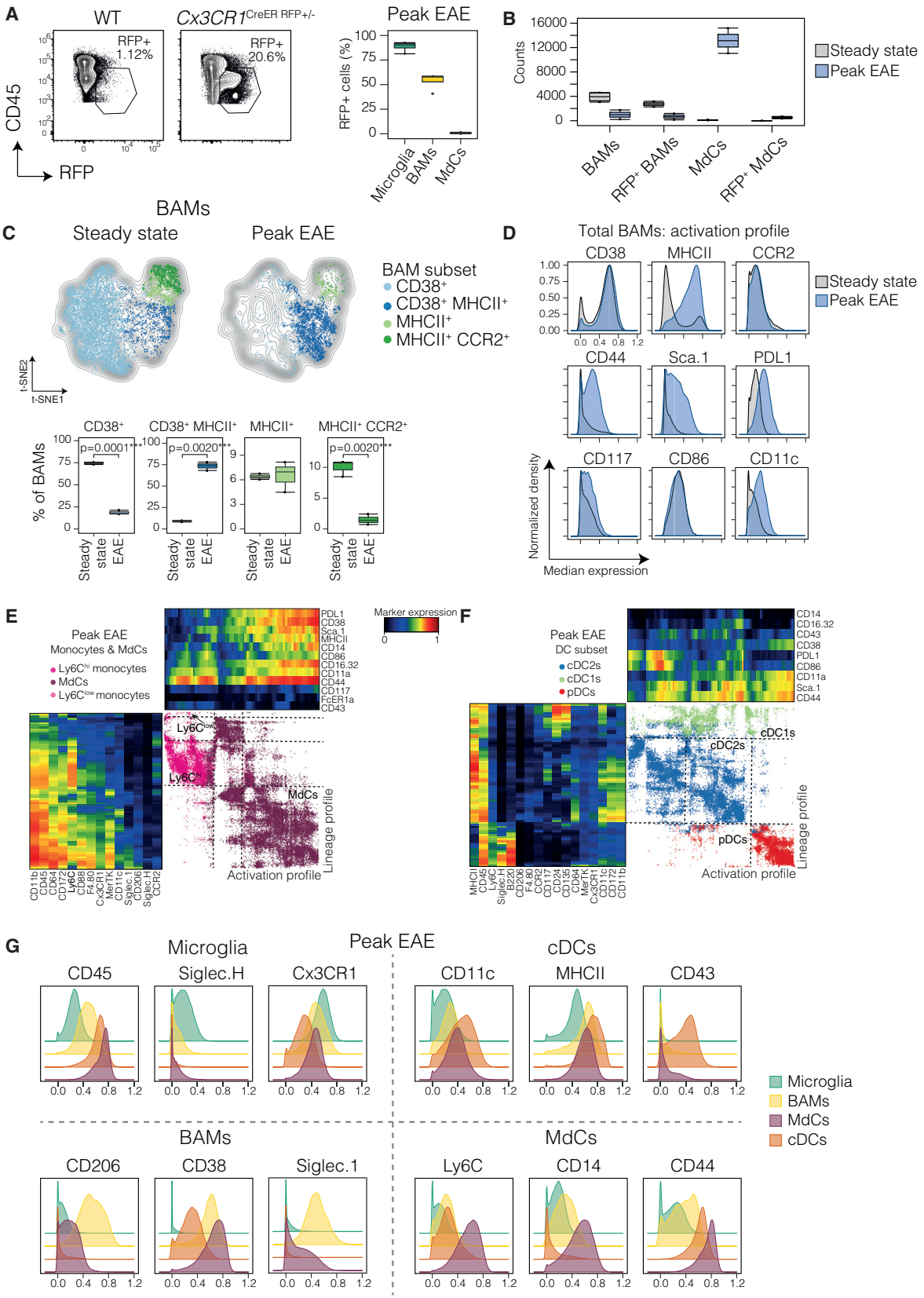

(legend on next page)

Besides BAMs, we were also able to discern multiple subsets of DCs within the steady-state CNS. Future studies should determine which of the identified CNS DC subsets sample CNS antigens and migrate to the draining cervical lymph nodes to activate naive T cells or Treg cells to maintain immune suppression. This is relevant during homeostasis, CNS infections, and neurodegeneration, where self, foreign, or pathogenic proteins may accumulate within the CNS parenchyma and meninges (Kalaria et al., 1996).

We extended our analysis to pathologic processes of aging and neurodegenerative disease. We identified a specific subset of reactive microglia associated with aging and AD. As we observed this microglial phenotype in geriatric WT mice and in relatively young APP/PS1 mice, this indicates that it may arise due to a specific response to cues from the local microenvironment rather than from cell-intrinsic aging. These cues may be similar in geriatric and APP/PS1 mice, e.g., myelin fragmentation (Safaiyan et al., 2016), protein accumulation (David, 2012), neurodegeneration (Krasemann et al., 2017; Wyss-Coray, 2016), and/or increased inflammatory mediators (Deleidi et al., 2015; Heppner et al., 2015). This is particularly supported by the increase in CD14 expression as CD14 is the co-receptor to the toll-like receptor 4 (TLR4) and together these receptors can be activated by amyloid-β (Reed-Geaghan et al., 2009) and upregulated by inflammatory cytokines like TNF-α (Zanoni et al., 2011). A recent report using sc-RNaseq of microglia showed that disease-associated microglia appear with disease progression in 5XFAD mice and have a phagocytic transcriptome signature (Keren-Shaul et al., 2017). However, regulation of mRNA and the encoded protein can differ dramatically and sc-RNaseq will, depending on the analysis depth, detect only abundant transcripts (Peterson et al., 2017). In support of this notion, many of the proteins we and others use to describe the CNS immune landscape did not overlap with the public sc-RNaseq data (https://www.ncbi.nlm.nih.gov/geo/query/acc.cgi?acc=GSE98969) (Keren-Shaul et al., 2017). Thus, our analysis provides surface protein markers, which can be targeted with commercially available mAbs, enabling cell isolation for further studies.

In contrast to neurodegenerative diseases, neuroinflammation is accompanied by a massive influx of immune infiltrates and dramatic changes in the CNS landscape. A recent report (Korin et al., 2017) suggested that all cells that are CD45^{hi} in the steady-state CNS are "CNS infiltrates." However, leukocytes in the steady-state CNS do not necessarily need to be immigrants. CNS infiltration into the parenchyma is a hallmark of neuro-inflammation (Becher et al., 2017). Furthermore, Korin et al. (2017) state that CD44 is a marker that distinguishes CNS-infiltrating cells from CNS-resident cells. In contrast, we found CD44 to be clearly expressed by steady-state CNS-resident leukocytes and further upregulated by microglia and BAMs during EAE, and by reactive microglia in aging and AD. Hence, our data suggest that CD44 alone is not a reliable marker to distinguish CNS-infiltrating cells from CNS-resident cells.

During EAE, we were able to discriminate subsets of infiltrating and resident myeloid cells and show that MdCs displayed a homogeneous macrophage-like phenotype, consistent with their role in myelin degradation and phagocytosis during EAE (Spath et al., 2017; Yamasaki et al., 2014). In contrast to high numbers of MdCs and cDCs, BAM numbers decreased during EAE, supporting the notion that tissue-resident macrophage numbers decline with the influx of peripheral inflammatory monocytes (Davies et al., 2013). At peak disease, BAMs lost their heterogeneity and almost exclusively co-expressed CD38 and MHCII. This BAM signature was also seen in geriatric mice to a lesser extent and may reflect a universal activation profile.

During EAE, microglia became skewed toward an entirely inflammatory phenotype. This phenotype bore some similarities to the signature in aging and AD-prone mice and may also in part represent a universal disease-associated microglial signature, as recently proposed (Krasemann et al., 2017; Zrzavy et al., 2017). However, EAE microglia also differed from the age and AD phenotype: EAE microglia dramatically upregulated MHCII and Sca-1, both IFN-γ-responsive genes, reflecting an interaction of microglia with CNS-invading T cells. Conversely, they did not upregulate CD14 while age- and AD-associated microglia did. In addition, the fact that the entire microglial population in the brain parenchyma became homogeneously reactive during EAE, compared to a small subpopulation of responsive microglia during aging and AD, is likely due to the great amount of cytokines and other inflammatory mediators delivered to the CNS by invading leukocytes during EAE (Becher et al., 2016, 2017). This also suggests that inflammatory EAE lesions affect microglia across the entire brain parenchyma even if they accumulate in the spinal cord, as is the case in EAE. Whereas we assume that microglia are not pathogenic per se, these global inflammation-induced changes in microglia may contribute to disease chronification, neurodegeneration, and brain atrophy, as observed in diseases like MS. In contrast, during aging and AD, the vast majority of microglia do not respond, demonstrating that neurodegeneration alone does not lead to the massive immune cell and cytokine influx into the CNS as seen in *bona fide* inflammatory diseases such as MS.

Taken together, our atlas identified distinct subsets of BAMs, steady-state and reactive subsets of microglia, and CNS DC subsets. We confirmed their identities by reporter and fate mapping, ontogeny, and responsiveness to growth factors. Using our steady-state map to interrogate the same leukocytes during pathology, we defined robust signatures for BAMs and microglia

Figure 7. BAMs Lose their Heterogeneity during Neuroinflammation but Are Still Distinguishable from MdCs and DCs

(A) CD45$^+$ CNS leukocytes (left) from *Cx3cr1*^{CreER} *Rosa26*-RFP and control mice at peak EAE, with quantification (right) of RFP$^+$ cells (n = 2, representative of two independent experiments).

(B) Total numbers of BAMs, RFP$^+$ BAMs, and MdCs in steady-state and peak EAE *Cx3cr1*^{CreER} *Rosa26*-RFP mice.

(C) BAM subset tSNE analysis by mass cytometry between steady-state and peak EAE mice.

(D) Highly upregulated makers between steady-state and peak EAE total BAMs.

(E and F) One-SENSE analysis of lineage and activation profiles of Ly6C^{hi} monocytes, MdCs, and Ly6C^{lo} monocytes (E) and DCs during peak EAE (F).

(G) Expression levels of distinguishing markers between microglia, BAMs, MdCs, and cDCs during peak EAE.

***p value significant (< 0.05) with a BH FDR < 1%. Error bars represent range. See also Figure S7.

during aging, neurodegeneration, and neuroinflammation. This atlas can now be used to target and isolate CNS leukocyte subsets with cell-surface protein markers in steady state and their specific disease-associated forms across pathologic conditions, thus enabling further studies into the role of these cells in maintaining CNS homeostasis and in the initiation or resolution of CNS disease.

STAR★METHODS

Detailed methods are provided in the online version of this paper and include the following:

- KEY RESOURCES TABLE
- CONTACT FOR REAGENT AND RESOURCE SHARING
- EXPERIMENTAL MODEL DETAILS
- METHOD DETAILS
  - *In vivo* treatments and EAE induction
  - Tissue harvesting and cell preparation
  - Mass cytometry
  - Fluorescence cytometry
  - Tracking intra-vascular cells in the CNS
  - Immunohistochemistry for BAMs
  - Immunohistochemistry for neutrophils
- QUANTIFICATION AND STATISTICAL ANALYSIS
  - Pre-processing of mass and flow cytometry data
  - Automated population identification in high-dimensional data analysis
  - Quantification of cells from immunohistochemistry
- DATA AND SOFTWARE AVAILABILITY

SUPPLEMENTAL INFORMATION

Supplemental Information includes seven figures and one table and can be found with this article online at https://doi.org/10.1016/j.immuni.2018.01.011.

ACKNOWLEDGMENTS

We thank the Mass- and Flow Cytometry Facility (University of Zurich) and the Center for Microscopy and Image Analysis (University of Zurich) for technical assistance; Lucy Robinson of Insight Editing London for critical review and editing of the manuscript; Nathalie Krakoski for discussions about BAMs; Nikolaus Deigendesch for APP/PS1 mouse transfers; Nir Yogev and Andrea Cogurra for discussions about all things meningeal; Will Macnair for comparison of protein and RNA expression; and Sarah Mundt for critical review and editing of the manuscript. This work was supported by grants from the Swiss national science foundation (PP00P3_144781 to M.G., 310030_146130, 316030_150768, 310030_170320 to B.B.), from the European Union: FP7 ITN_NeuroKine (B.B.) and FP7 Project ATECT (B.B.), from the University Priority Project Translational Cancer Research (B.B.), from the National Science Foundation Graduate Research Fellowship Program (DGE1418060) (B.P.L.), and the Forschungskredit awarded by the University of Zurich to D. Mrdjen.

AUTHOR CONTRIBUTIONS

D. Mrdjen and B.B. conceived the study. D. Mrdjen performed all cytometry experiments with help from A.P. with fluorescence cytometry experiments. D. Mrdjen performed all data analysis and representation with help from F.J.H. S.G.U., B.S., and D. Merkler performed imaging experiments. S.G.U. performed quantification of imaging data. I.L. and B.P.L. helped with experiment in APP/PS1 mice. F.L.H. provided APP/PS1 mice. D. Mrdjen and B.B. wrote the manuscript with input from F.J.H., J.K., D. Merkler, and M.G. B.B. financed and supervised the study.

DECLARATION OF INTERESTS

The authors declare no competing interests.

Received: September 26, 2017
Revised: December 5, 2017
Accepted: January 14, 2018
Published: February 6, 2018; corrected online: March 6, 2018

REFERENCES

Anandasabapathy, N., Victora, G.D., Meredith, M., Feder, R., Dong, B., Kluger, C., Yao, K., Dustin, M.L., Nussenzweig, M.C., Steinman, R.M., and Liu, K. (2011). Flt3L controls the development of radiosensitive dendritic cells in the meninges and choroid plexus of the steady-state mouse brain. J. Exp. Med. *208*, 1695–1705.

Anderson, K.G., Mayer-Barber, K., Sung, H., Beura, L., James, B.R., Taylor, J.J., Qunaj, L., Griffith, T.S., Vezys, V., Barber, D.L., and Masopust, D. (2014). Intravascular staining for discrimination of vascular and tissue leukocytes. Nat. Protoc. *9*, 209–222.

Aspelund, A., Antila, S., Proulx, S.T., Karlsen, T.V., Karaman, S., Detmar, M., Wiig, H., and Alitalo, K. (2015). A dural lymphatic vascular system that drains brain interstitial fluid and macromolecules. J. Exp. Med. *212*, 991–999.

Bandura, D.R., Baranov, V.I., Ornatsky, O.I., Antonov, A., Kinach, R., Lou, X., Pavlov, S., Vorobiev, S., Dick, J.E., and Tanner, S.D. (2009). Mass cytometry: technique for real time single cell multitarget immunoassay based on inductively coupled plasma time-of-flight mass spectrometry. Anal. Chem. *81*, 6813–6822.

Baruch, K., Ron-Harel, N., Gal, H., Deczkowska, A., Shifrut, E., Ndifon, W., Mirlas-Neisberg, N., Cardon, M., Vaknin, I., Cahalon, L., et al. (2013). CNS-specific immunity at the choroid plexus shifts toward destructive Th2 inflammation in brain aging. Proc. Natl. Acad. Sci. USA *110*, 2264–2269.

Becher, B., Schlitzer, A., Chen, J., Mair, F., Sumatoh, H.R., Teng, K.W., Low, D., Ruedl, C., Riccardi-Castagnoli, P., Poidinger, M., et al. (2014). High-dimensional analysis of the murine myeloid cell system. Nat. Immunol. *15*, 1181–1189.

Becher, B., Tugues, S., and Greter, M. (2016). GM-CSF: from growth factor to central mediator of tissue inflammation. Immunity *45*, 963–973.

Becher, B., Spath, S., and Goverman, J. (2017). Cytokine networks in neuroinflammation. Nat. Rev. Immunol. *17*, 49–59.

Bechmann, I., Kwidzinski, E., Kovac, A.D., Simbürger, E., Horvath, T., Gimsa, U., Dirnagl, U., Priller, J., and Nitsch, R. (2001). Turnover of rat brain perivascular cells. Exp. Neurol. *168*, 242–249.

Bendall, S.C., Simonds, E.F., Qiu, P., Amir, A.D., Krutzik, P.O., Finck, R., Bruggner, R.V., Melamed, R., Trejo, A., Ornatsky, O.I., et al. (2011). Single-cell mass cytometry of differential immune and drug responses across a human hematopoietic continuum. Science *332*, 687–696.

Buttgereit, A., Lelios, I., Yu, X., Vrohlings, M., Krakoski, N.R., Gautier, E.L., Nishinakamura, R., Becher, B., and Greter, M. (2016). Sall1 is a transcriptional regulator defining microglia identity and function. Nat. Immunol. *17*, 1397–1406.

Cheng, Y., Wong, M.T., van der Maaten, L., and Newell, E.W. (2016). Categorical analysis of human T cell heterogeneity with one-dimensional soli-expression by nonlinear stochastic embedding. J. Immunol. *196*, 924–932.

Clemente-Casares, X., Hosseinzadeh, S., Barbu, I., Dick, S.A., Macklin, J.A., Wang, Y., Momen, A., Kantores, C., Aronoff, L., Farno, M., et al. (2017). A CD103+ conventional dendritic cell surveillance system prevents development of overt heart failure during subclinical viral myocarditis. Immunity *47*, 974–989.e8.

Codarri, L., Greter, M., and Becher, B. (2013). Communication between pathogenic T cells and myeloid cells in neuroinflammatory disease. Trends Immunol. *34*, 114–119.

Colonna, M., and Butovsky, O. (2017). Microglia function in the central nervous system during health and neurodegeneration. Annu. Rev. Immunol. *35*, 441–468.

Croxford, A.L., Lanzinger, M., Hartmann, F.J., Schreiner, B., Mair, F., Pelczar, P., Clausen, B.E., Jung, S., Greter, M., and Becher, B. (2015a). The cytokine GM-CSF drives the inflammatory signature of CCR2+ monocytes and licenses autoimmunity. Immunity *43*, 502–514.

Croxford, A.L., Spath, S., and Becher, B. (2015b). GM-CSF in neuroinflammation: licensing myeloid cells for tissue damage. Trends Immunol. *36*, 651–662.

David, D.C. (2012). Aging and the aggregating proteome. Front. Genet. *3*, 247.

Davies, L.C., Jenkins, S.J., Allen, J.E., and Taylor, P.R. (2013). Tissue-resident macrophages. Nat. Immunol. *14*, 986–995.

Deleidi, M., Jäggle, M., and Rubino, G. (2015). Immune aging, dysmetabolism, and inflammation in neurological diseases. Front. Neurosci. *9*, 172.

Engelhardt, B., Vajkoczy, P., and Weller, R.O. (2017). The movers and shapers in immune privilege of the CNS. Nat. Immunol. *18*, 123–131.

Finck, R., Simonds, E.F., Jager, A., Krishnaswamy, S., Sachs, K., Fantl, W., Pe'er, D., Nolan, G.P., and Bendall, S.C. (2013). Normalization of mass cytometry data with bead standards. Cytometry A *83*, 483–494.

Ginhoux, F., Greter, M., Leboeuf, M., Nandi, S., See, P., Gokhan, S., Mehler, M.F., Conway, S.J., Ng, L.G., Stanley, E.R., et al. (2010). Fate mapping analysis reveals that adult microglia derive from primitive macrophages. Science *330*, 841–845.

Goldmann, T., Wieghofer, P., Jordão, M.J.C., Prutek, F., Hagemeyer, N., Frenzel, K., Amann, L., Staszewski, O., Kierdorf, K., Krueger, M., et al. (2016). Origin, fate and dynamics of macrophages at central nervous system interfaces. Nat. Immunol. *17*, 797–805.

Greter, M., Heppner, F.L., Lemos, M.P., Odermatt, B.M., Goebels, N., Laufer, T., Noelle, R.J., and Becher, B. (2005). Dendritic cells permit immune invasion of the CNS in an animal model of multiple sclerosis. Nat. Med. *11*, 328–334.

Greter, M., Lelios, I., and Croxford, A.L. (2015). Microglia versus myeloid cell nomenclature during brain inflammation. Front. Immunol. *6*, 249.

Guilliams, M., Dutertre, C.-A., Scott, C.L., McGovern, N., Sichien, D., Chakarov, S., Van Gassen, S., Chen, J., Poidinger, M., De Prijck, S., et al. (2016). Unsupervised high-dimensional analysis aligns dendritic cells across tissues and species. Immunity *45*, 669–684.

Hanisch, U.K., and Kettenmann, H. (2007). Microglia: active sensor and versatile effector cells in the normal and pathologic brain. Nat. Neurosci. *10*, 1387–1394.

Hartmann, F.J., Bernard-Valnet, R., Quériault, C., Mrdjen, D., Weber, L.M., Galli, E., Krieg, C., Robinson, M.D., Nguyen, X.-H., Dauvilliers, Y., et al. (2016). High-dimensional single-cell analysis reveals the immune signature of narcolepsy. J. Exp. Med. *213*, 2621–2633.

Heppner, F.L., Ransohoff, R.M., and Becher, B. (2015). Immune attack: the role of inflammation in Alzheimer disease. Nat. Rev. Neurosci. *16*, 358–372.

Herz, J., Filiano, A.J., Smith, A., Yogev, N., and Kipnis, J. (2017). Myeloid cells in the central nervous system. Immunity *46*, 943–956.

Hoeffel, G., Chen, J., Lavin, Y., Low, D., Almeida, F.F., See, P., Beaudin, A.E., Lum, J., Low, I., Forsberg, E.C., et al. (2015). C-Myb(+) erythro-myeloid progenitor-derived fetal monocytes give rise to adult tissue-resident macrophages. Immunity *42*, 665–678.

Kalaria, R.N., Premkumar, D.R.D., Pax, A.B., Cohen, D.L., and Lieberburg, I. (1996). Production and increased detection of amyloid β protein and amyloidogenic fragments in brain microvessels, meningeal vessels and choroid plexus in Alzheimer's disease. Brain Res. Mol. Brain Res. *35*, 58–68.

Keren-Shaul, H., Spinrad, A., Weiner, A., Matcovitch-Natan, O., Dvir-Szternfeld, R., Ulland, T.K., David, E., Baruch, K., Lara-Astaiso, D., Toth, B., et al. (2017). A unique microglia type associated with restricting development of Alzheimer's disease. Cell *169*, 1276–1290.e17.

Kettenmann, H., Kirchhoff, F., and Verkhratsky, A. (2013). Microglia: new roles for the synaptic stripper. Neuron *77*, 10–18.

Kivisäkk, P., Imitola, J., Rasmussen, S., Elyaman, W., Zhu, B., Ransohoff, R.M., and Khoury, S.J. (2009). Localizing central nervous system immune surveillance: meningeal antigen-presenting cells activate T cells during experimental autoimmune encephalomyelitis. Ann. Neurol. *65*, 457–469.

Korin, B., Ben-Shaanan, T.L., Schiller, M., Dubovik, T., Azulay-Debby, H., Boshnak, N.T., Koren, T., and Rolls, A. (2017). High-dimensional, single-cell characterization of the brain's immune compartment. Nat. Neurosci. *20*, 1300–1309.

Kotecha, N., Krutzik, P.O., and Irish, J.M. (2010). Web-based analysis and publication of flow cytometry experiments. In Current Protocols in Cytometry (Hoboken, NJ, USA: John Wiley & Sons, Inc.).

Krasemann, S., Madore, C., Cialic, R., Baufeld, C., Calcagno, N., El Fatimy, R., Beckers, L., O'Loughlin, E., Xu, Y., Fanek, Z., et al. (2017). The TREM2-APOE pathway drives the transcriptional phenotype of dysfunctional microglia in neurodegenerative diseases. Immunity *47*, 566–581.e9.

Levine, J.H., Simonds, E.F., Bendall, S.C., Davis, K.L., Amir, A.D., Tadmor, M.D., Litvin, O., Fienberg, H.G., Jager, A., Zunder, E.R., et al. (2015). Data-driven phenotypic dissection of AML reveals progenitor-like cells that correlate with prognosis. Cell *162*, 184–197.

Louveau, A., Smirnov, I., Keyes, T.J., Eccles, J.D., Rouhani, S.J., Peske, J.D., Derecki, N.C., Castle, D., Mandell, J.W., Lee, K.S., et al. (2015). Structural and functional features of central nervous system lymphatic vessels. Nature *523*, 337–341.

Mair, F., Hartmann, F.J., Mrdjen, D., Tosevski, V., Krieg, C., and Becher, B. (2016). The end of gating? An introduction to automated analysis of high dimensional cytometry data. Eur. J. Immunol. *46*, 34–43.

Maraskovsky, E., Brasel, K., Teepe, M., Roux, E.R., Lyman, S.D., Shortman, K., and McKenna, H.J. (1996). Dramatic increase in the numbers of functionally mature dendritic cells in Flt3 ligand-treated mice: multiple dendritic cell subpopulations identified. J. Exp. Med. *184*, 1953–1962.

Mei, H.E., Leipold, M.D., Schulz, A.R., Chester, C., and Maecker, H.T. (2015). Barcoding of live human peripheral blood mononuclear cells for multiplexed mass cytometry. J. Immunol. *194*, 2022–2031.

Merad, M., and Manz, M.G. (2009). Dendritic cell homeostasis. Blood *113*, 3418–3427.

Mrdjen, D., Hartmann, F.J., and Becher, B. (2017). High dimensional cytometry of central nervous system leukocytes during neuroinflammation. In Inflammation: Methods and Protocols, B.E. Clausen and J.D. Laman, eds. (New York, NY: Springer New York), pp. 321–332.

Murphy, J.B., and Sturm, E. (1923). Conditions determining the transplantability of tissues in the brain. J. Exp. Med. *38*, 183–197.

Perry, V.H., and Holmes, C. (2014). Microglial priming in neurodegenerative disease. Nat. Rev. Neurol. *10*, 217–224.

Peterson, V.M., Zhang, K.X., Kumar, N., Wong, J., Li, L., Wilson, D.C., Moore, R., McClanahan, T.K., Sadekova, S., and Klappenbach, J.A. (2017). Multiplexed quantification of proteins and transcripts in single cells. Nat. Biotechnol. *35*, 936–939.

Prinz, M., and Priller, J. (2014). Microglia and brain macrophages in the molecular age: from origin to neuropsychiatric disease. Nat. Rev. Neurosci. *15*, 300–312.

Prokop, S., Miller, K.R., Drost, N., Handrick, S., Mathur, V., Luo, J., Wegner, A., Wyss-Coray, T., and Heppner, F.L. (2015). Impact of peripheral myeloid cells on amyloid-β pathology in Alzheimer's disease-like mice. J. Exp. Med. *212*, 1811–1818.

Radde, R., Bolmont, T., Kaeser, S.A., Coomaraswamy, J., Lindau, D., Stoltze, L., Calhoun, M.E., Jäggi, F., Wolburg, H., Gengler, S., et al. (2006). Abeta42-driven cerebral amyloidosis in transgenic mice reveals early and robust pathology. EMBO Rep. *7*, 940–946.

Reed-Geaghan, E.G., Savage, J.C., Hise, A.G., and Landreth, G.E. (2009). CD14 and toll-like receptors 2 and 4 are required for fibrillar Abeta-stimulated microglial activation. J. Neurosci. *29*, 11982–11992.

Ritzel, R.M., Crapser, J., Patel, A.R., Verma, R., Grenier, J.M., Chauhan, A., Jellison, E.R., and McCullough, L.D. (2016). Age-associated resident memory CD8 T cells in the central nervous system are primed to potentiate inflammation after ischemic brain injury. J. Immunol. *196*, 3318–3330.

Safaiyan, S., Kannaiyan, N., Snaidero, N., Brioschi, S., Biber, K., Yona, S., Edinger, A.L., Jung, S., Rossner, M.J., and Simons, M. (2016). Age-related myelin degradation burdens the clearance function of microglia during aging. Nat. Neurosci. *19*, 995–998.

Salter, M.W., and Beggs, S. (2014). Sublime microglia: expanding roles for the guardians of the CNS. Cell *158*, 15–24.

Schläger, C., Körner, H., Krueger, M., Vidoli, S., Haberl, M., Mielke, D., Brylla, E., Issekutz, T., Cabañas, C., Nelson, P.J., et al. (2016). Effector T-cell trafficking between the leptomeninges and the cerebrospinal fluid. Nature *530*, 349–353.

Schlitzer, A., McGovern, N., Teo, P., Zelante, T., Atarashi, K., Low, D., Ho, A.W., See, P., Shin, A., Wasan, P.S., et al. (2013). IRF4 transcription factor-dependent CD11b+ dendritic cells in human and mouse control mucosal IL-17 cytokine responses. Immunity *38*, 970–983.

Schreiner, B., Heppner, F.L., and Becher, B. (2009). Modeling multiple sclerosis in laboratory animals. Semin. Immunopathol. *31*, 479–495.

Schulz, C., Gomez Perdiguero, E., Chorro, L., Szabo-Rogers, H., Cagnard, N., Kierdorf, K., Prinz, M., Wu, B., Jacobsen, S.E., Pollard, J.W., et al. (2012). A lineage of myeloid cells independent of Myb and hematopoietic stem cells. Science *336*, 86–90.

Shechter, R., Miller, O., Yovel, G., Rosenzweig, N., London, A., Ruckh, J., Kim, K.W., Klein, E., Kalchenko, V., Bendel, P., et al. (2013). Recruitment of beneficial M2 macrophages to injured spinal cord is orchestrated by remote brain choroid plexus. Immunity *38*, 555–569.

Shirai, Y. (1921). On the transplant of the rat sarcoma in adult heterogenous animals. Japan Medical World *1921*, 14–15.

Spath, S., Komuczki, J., Hermann, M., Pelczar, P., Mair, F., Schreiner, B., and Becher, B. (2017). Dysregulation of the cytokine GM-CSF induces spontaneous phagocyte invasion and immunopathology in the central nervous system. Immunity *46*, 245–260.

Spitzer, M.H., Gherardini, P.F., Fragiadakis, G.K., Bhattacharya, N., Yuan, R.T., Hotson, A.N., Finck, R., Carmi, Y., Zunder, E.R., Fantl, W.J., et al. (2015). IMMUNOLOGY. An interactive reference framework for modeling a dynamic immune system. Science *349*, 1259425.

Streit, W.J., Braak, H., Xue, Q.S., and Bechmann, I. (2009). Dystrophic (senescent) rather than activated microglial cells are associated with tau pathology and likely precede neurodegeneration in Alzheimer's disease. Acta Neuropathol. *118*, 475–485.

Van Der Maaten, L., and Hinton, G. (2008). Visualizing data using t-SNE. J. Mach. Learn. Res. *9*, 2579–2605.

Van Gassen, S., Callebaut, B., Van Helden, M.J., Lambrecht, B.N., Demeester, P., Dhaene, T., and Saeys, Y. (2015). FlowSOM: Using self-organizing maps for visualization and interpretation of cytometry data. Cytometry A *87*, 636–645.

Vom Berg, J., Prokop, S., Miller, K.R., Obst, J., Kälin, R.E., Lopategui-Cabezas, I., Wegner, A., Mair, F., Schipke, C.G., Peters, O., et al. (2012). Inhibition of IL-12/IL-23 signaling reduces Alzheimer's disease-like pathology and cognitive decline. Nat. Med. *18*, 1812–1819.

Wyss-Coray, T. (2016). Ageing, neurodegeneration and brain rejuvenation. Nature *539*, 180–186.

Yamasaki, R., Lu, H., Butovsky, O., Ohno, N., Rietsch, A.M., Cialic, R., Wu, P.M., Doykan, C.E., Lin, J., Cotleur, A.C., et al. (2014). Differential roles of microglia and monocytes in the inflamed central nervous system. J. Exp. Med. *211*, 1533–1549.

Yona, S., Kim, K.W., Wolf, Y., Mildner, A., Varol, D., Breker, M., Strauss-Ayali, D., Viukov, S., Guilliams, M., Misharin, A., et al. (2013). Fate mapping reveals origins and dynamics of monocytes and tissue macrophages under homeostasis. Immunity *38*, 79–91.

Yuri, S., Fujimura, S., Nimura, K., Takeda, N., Toyooka, Y., Fujimura, Y., Aburatani, H., Ura, K., Koseki, H., Niwa, H., and Nishinakamura, R. (2009). Sall4 is essential for stabilization, but not for pluripotency, of embryonic stem cells by repressing aberrant trophectoderm gene expression. Stem Cells *27*, 796–805.

Zanoni, I., Ostuni, R., Marek, L.R., Barresi, S., Barbalat, R., Barton, G.M., Granucci, F., and Kagan, J.C. (2011). CD14 controls the LPS-induced endocytosis of Toll-like receptor 4. Cell *147*, 868–880.

Zrzavy, T., Hametner, S., Wimmer, I., Butovsky, O., Weiner, H.L., and Lassmann, H. (2017). Loss of 'homeostatic' microglia and patterns of their activation in active multiple sclerosis. Brain *140*, 1900–1913.

STAR★METHODS

KEY RESOURCES TABLE

REAGENT or RESOURCE	SOURCE	IDENTIFIER
Antibodies		
anti-mouse CD45 clone 30-F11, 104-Pd	BioLegend	Cat # 103102; RRID: AB_312967
anti-mouse CD45 clone 30-F11, 105-Pd	BioLegend	Cat # 103102; RRID: AB_312967
anti-mouse CD45 clone 30-F11, 106-Pd	BioLegend	Cat # 103102; RRID: AB_312967
anti-mouse CD45 clone 30-F11, 108-Pd	BioLegend	Cat # 103102; RRID: AB_312967
anti-mouse CD45 clone 30-F11, 110-Pd	BioLegend	Cat # 103102; RRID: AB_312967
anti-mouse Ly6G clone 1A8, 141-Pr	Fluidigm	Cat# 3141008B
anti-mouse Cx3CR1 clone SA011F11, 142-Nd	BioLegend	Cat# 149002; RRID: AB_2564313
anti-mouse CD88 clone 20/70, 143-Nd	BioLegend	Cat# 135802; RRID: AB_1953295
anti-mouse CD11a clone M17/4, 144-Nd	Bio X Cell	Cat# BE0006; RRID: AB_1107578
anti-mouse Siglec-F clone E50-2440, 145-Nd	BD Biosciences	Cat# 552125; RRID: AB_394340
anti-mouse CD11c clone N418, 146-Nd	BioLegend	Cat# 117302; RRID: AB_313771
anti-mouse CD45 clone 30-F11, 147-Sm	Fluidigm	Cat# 3147003B
anti-mouse CD11b clone M1/70, 148-Nd	Fluidigm	Cat# 3148003B
anti-mouse B220 clone RA3.3A1, 149-Sm	Bio X Cell	Cat# BE0067; RRID: AB_1107651
anti-mouse Ly6C clone HK1.4, 150-Nd	Fluidigm	Cat# 3150010B
anti-mouse CD64 clone X54-5/7.1, 151-Eu	Fluidigm	Cat# 3151012B
anti-mouse CD3 clone 145-2C11, 152-Sm	Fluidigm	Cat# 3152004B
anti-mouse PDL1 clone 10F.9G2, 153-Eu	Bio X Cell	Cat# BE0101; RRID: AB_10949073
anti-mouse Ter119 clone TER-119, 154-Sm	Fluidigm	Cat# 3154005B
anti-mouse CD90 clone T24/31, 155-Gd	Bio X Cell	Cat# BE0212; RRID: AB_2687698
anti-mouse CD14 clone Sa14-2, 156-Gd	Fluidigm	Cat# 3156009B
anti-mouse Siglec-H clone 551, 158-Gd	BioLegend	Cat# 129602; RRID: AB_1227757
anti-mouse Siglec-1 clone 3D6.112, 159-Tb	BioLegend	Cat# 142402; RRID: AB_10916523
anti-mouse MerTK polyclonal, biotin	R&D Systems	Cat# BAF591; RRID: AB_2098563
anti-mouse CD135 clone A2F10, 161-Dy	eBioscience	Cat# 14-1351-82; RRID: AB_467481
anti-mouse CD24 clone J11d, 162-Dy	Bio X Cell	Cat# BE0227; RRID: AB_2687710
anti-mouse CCR2 clone 475301, APC	R&D Systems	Cat# FAB5538A; RRID: AB_10645617
anti-mouse F4/80 clone Cl:A3-1, 164-Dy	BioRad	Cat# MCA497G; RRID: AB_872005
anti-mouse CD38 clone 90, 165-Ho	BioLegend	Cat# 102702; RRID: AB_312923
anti-mouse CD117 clone 2B8, 166-Er	Fluidigm	Cat# 3166004B
anti-mouse CD16/32 clone 93, 167-Er	BioLegend	Cat# 101302; RRID: AB_312801
anti-mouse CD206 clone CO8C2, 168-Er	BioLegend	Cat# 14170210900233
anti-mouse Sca-1 clone D7, 169-Tm	Fluidigm	Cat# 3169015B
anti-mouse NK1.1 clone PK136, 170-Er	BioLegend	Cat# 108702; RRID: AB_313389
anti-mouse/human CD44 clone IM7, 171-Yb	Fluidigm	Cat# 3171003B
anti-mouse CD86 clone GL-1, 172-Yb	Bio X Cell	Cat# BE0025; RRID: AB_1107678
anti-mouse CD172 clone P84, 173-Yb	BioLegend	Cat# 144002; RRID: AB_11203711
anti-mouse MHCII clone M5/114.15.2, 174-Yb	Fluidigm	Cat# 3174003B
anti-mouse CD43 clone 1B11, 175-Lu	BioLegend	Cat# 121202; RRID: AB_493382
anti-mouse FcER1a clone MAR-1, 176-Yb	BioLegend	Cat# 1343021626078
anti-APC clone APC003, 163-Dy	BioLegend	Cat# 409002; RRID: AB_345357
anti-biotin clone 1D4-C5, 160-Dy	BioLegend	Cat# 408002; RRID: AB_10642032
anti-GFP clone 1GFP63, 163-Dy	BioLegend	Cat# 668205; RRID: AB_2616789

(*Continued on next page*)

Continued

REAGENT or RESOURCE	SOURCE	IDENTIFIER
anti-mouse CD38 clone 90, Alexa Fluor 488	BioLegend	Cat# 102714; RRID: AB_528796
anti-mouse CD88 clone 20/70, Biotin	BioLegend	Cat# 135811; RRID: AB_11149683
anti-mouse CD24 clone M1/69, Brilliant Ultra Violet 496	BD	Cat# 564664; RRID: AB_2716853
anti-mouse Ly6G clone 1A8, Brilliant Ultra Violet 563	BD	Cat# 565707
anti-mouse CD11b clone M1/70, Brilliant Ultra Violet 661	BD	Cat# 565080
anti-mouse CD11b clone M1/70, Brilliant Ultra Violet 737	BD	Cat# 564443
anti-mouse CD11b clone M1/70, APC	BD	Cat# 101212; RRID: AB_312795
anti-mouse F4/80 clone BM8, Brilliant Violet 421	BioLegend	Cat# 123137; RRID: AB_2563102
anti-mouse F4/80 clone BM8, Brilliant Violet 510	BioLegend	Cat# 123135; RRID: AB_2562622
anti-mouse CD206 clone C068C2, Brilliant Violet 605	BioLegend	Cat# 141721; RRID: AB_2562340
anti-mouse CD206 clone C068C2, Alexa Fluor 700	BioLegend	Cat# 141733; RRID: AB_2629636
anti-mouse Ly6C clone HK1.4, Brilliant Violet 711	BioLegend	Cat# 128037; RRID: AB_2562630
anti-mouse Lyve1 clone ALY7, eFlour 660	eBioscience	Cat# 50-0443-82; RRID: AB_10597449
anti-mouse CD90.2 clone 30-H12, Brilliant Violet 785	BioLegend	Cat# 105331; RRID: AB_2562900
anti-mouse CD90.2 clone 30-H12, Brilliant Violet 605	BioLegend	Cat# 105343; RRID: AB_2632889
anti-mouse CD45 clone 30-F11, Brilliant Ultra Violet 395	BD	Cat# 564279; RRID: AB_2651134
anti-mouse CD45 clone 30-F11, PE-Cy5	BD	Cat# 553082; RRID: AB_394612
anti-mouse CD45 clone 30-F11, Pacific Blue	BioLegend	Cat# 103126; RRID: AB_493535
anti-mouse CD11c clone N418, PE-Cy5.5	eBioscience	Cat# 35-0114-82; RRID: AB_469709
anti-mouse MerTK clone DS5MMER, PE-Cy7	eBioscience	Cat# 25-5751-82; RRID: AB_2573466
anti-mouse CX3CR1 clone SA011F11, PE-Dazzle 594	BioLegend	Cat# 149013; RRID: AB_2565697
anti-mouse CD44 clone IM7, Brilliant Ultra Violet 737	BD	Cat# 564392
anti-mouse CD44 clone IM7, Brilliant Violet 650	BioLegend	Cat# 103049; RRID: AB_2562600
anti-mouse CD4 clone RM4-5, Brilliant Violet 650	BioLegend	Cat# 100546; RRID: AB_2562098
anti-mouse CD8a clone 53-6.7, Brilliant Ultra Violet 805	BD	Cat# 564920; RRID: AB_2716856
anti-mouse CD3 clone 145-2C11, Brilliant Violet 421	BioLegend	Cat# 100341; RRID: AB_2562556
anti-mouse CD3 clone 17A2, Alexa Flour 700	eBioscience	Cat# 56-0032-82; RRID: AB_529507
anti-mouse CD3 clone 17A2, Brilliant Ultra Violet 737	BD	Cat# 564380
anti-mouse CD3 clone 17A2, Brilliant Ultra Violet 395	BD	Cat# 740268; RRID: AB_2687927
anti-mouse B220 clone RA3-6B2, APC	BioLegend	Cat# 103212; RRID: AB_312997
anti-mouse B220 clone RA3-6B2, Brilliant Violet 785	BioLegend	Cat# 103205; RRID: AB_312990
anti-mouse MHCII clone M5/114.15.2, Alexa Flour 700	BioLegend	Cat# 107622; RRID: AB_493727
anti-mouse MHCII clone M5/114.15.2, Pacific blue	BioLegend	Cat# 107620; RRID: AB_493527
anti-mouse MHCII clone M5/114.15.2, Brilliant Blue 700	BD	Cat# 746197
anti-mouse Siglec-H clone 551, PE	eBioscience	Cat# 12-0333-82; RRID: AB_10597139
anti-mouse NK1.1 clone PK136, PE	BD	Cat# 553165; RRID: AB_394677
rat IgG2bk isotype control clone rtk4530, Pacific blue	BioLegend	Cat# 400627; RRID: AB_493561
Streptavidin polyclonal, Brilliant Ultra Violet 661	BD	Cat# 565081
Streptavidin polyclonal, PE-Cy5	BD	Cat# 554062; RRID: AB_10053563
anti-mouse Iba1 clone 019-19741	Wako	Cat# 019-19741; RRID: AB_839504
anti-mouse MHCII clone M5/114.15.2, Alexa Fluor 488	Biolegend	Cat# 107616; RRID: AB_493523
anti-mouse CD206 clone MR5D3, Biotin	Bio-Rad	Cat# MCA2235BT; RRID: AB_1101315
anti-mouse CD11c clone N418, APC	BioLegend	Cat# 117310; RRID: AB_313779
anti-mouse Collagen IV polyclonal	Bio-Rad	Cat# 2150-1470; RRID: AB_2082660
goat anti-rabbit polyclonal, Alexa Fluor 546	Thermo Fisher	Cat# A11010; RRID: AB_2534077
goat anti-rabbit polyclonal, Alexa Fluor 488	Thermo Fisher	Cat# A11034; RRID: AB_2576217
goat anti-rat polyclonal, Alexa Fluor 647	Thermo Fisher	Cat# A21247; RRID: AB_141778
goat anti-rat polyclonal, Alexa Fluor 488	Thermo Fisher	Cat# A11006; RRID: AB_2534074
goat anti-rat polyclonal, Cy3	Life Technologies	Cat# A11034; RRID: AB_2576217

(*Continued on next page*)

Continued

REAGENT or RESOURCE	SOURCE	IDENTIFIER
goat anti-hamster polyclonal, Alexa Fluor 546	Thermo Fisher	Cat# A21111; RRID: AB_2535760
donkey anti-rabbit polyclonal, Alexa Fluor 555	Jackson	Cat# 712-165-153; RRID: AB_2340667
Streptavidin polyclonal, Alexa Fluor 488	Thermo Fisher	Cat# S112223; RRID: AB_2336881
Streptavidin polyclonal, Alexa Fluor 647	Thermo Fisher	Cat# S32357; RRID: AB_2336066
anti-mouse Ly6G clone 1A8, purified	BioLegend	Cat# 127602; RRID: AB_1089180
Chemicals, Peptides, and Recombinant Proteins		
vWF	Abcam	Cat# ab6994; RRID: AB_305689
DAPI	Life Technologies	Cat# D3571; RRID: AB_2307445
FLt3L	Bio X Cell	Cat # BE0098; RRID: AB_10949072
anti-CSF1R clone AFS98	Bio X Cell	Cat# BE0213; RRID: AB_2687699
Zombie NIR dye	Biolegend	Cat# 423106
Iridium	Sigma	Cat# 520721
Cisplatin	Sigma	Cat# P4394
MAXPAR Fix/Perm buffer	Fluidigm	Cat# 201067
MAXPAR water	Fluidigm	Cat# 201069
USEDECALC solution	MEDITE	Cat# 40-3310-00
Perm wash	Home-made	N/A
Palladium 104, 105, 106, 108, 110	Trace	N/A
Metal labeling kits	Fluidigm	N/A
normal goat serum	Life Technologies	Cat# PCN500
PBS	Homemade	N/A
Percoll	GE	Cat# P4937
Deposited Data		
CyTOF data from C57BL/6 mice	This paper	https://community.cytobank.org/cytobank/experiments/69323
CyTOF data from APP/PS1 mice and littermate controls	This paper	https://community.cytobank.org/cytobank/experiments/69324
Software and Algorithms		
FlowJo v10.2	Tree Star	https://www.flowjo.com/
Cytobank	Kotecha et al., 2010	https://www.cytobank.org/
MATLAB R2016a	N/A	https://www.mathworks.com/
Normalizer	Finck et al., 2013	https://github.com/nolanlab/bead-normalization/releases
t-SNE	Van Der Maaten and Hinton, 2008	https://github.com/jkrijthe/Rtsne
FlowSOM	Van Gassen et al., 2015	https://github.com/SofieVG/FlowSOM
Scaffold	Spitzer et al., 2015	https://github.com/nolanlab/scaffold
One-SENSE	Cheng et al., 2016	N/A
R	R Development Core Team, 2008	https://www.r-project.org/
R Studio	N/A	https://www.rstudio.com/

CONTACT FOR REAGENT AND RESOURCE SHARING

Further information and requests for reagents should be directed to and will be fulfilled by Lead Contact Burkhard Becher (becher@immunology.uzh.ch).

EXPERIMENTAL MODEL DETAILS

C57BL/6 (wild-type) mice were purchased from Janvier Laboraories and were taken to adulthood at 8 weeks of age or to geriatric age at 1.5 years of age and tissues were harvested together. *Sall-1*^{GFP} reporter mice were described previously (Yuri et al., 2009). *Cx3cr1*^{CreER} *Rosa26*-RFP fatemap mice were kindly provided by S. Jung (Weizmann Institute of Science) (Yona et al.,

2013). Heterozygous APP/PS1 mice which overexpress the familial AD mutant form of human APP (the Swedish mutation, K670N/M671L) and PS1 (M146L/L286V) transgenes under the transcriptional control of the neuron-specific mouse Thy-1 promoter (Radde et al., 2006), and littermate controls, aged 4 months were kindly provided by F. Heppner (Charité–Universitätsmedizin Berlin). All animal experiments performed in this study were approved by the Cantonal Veterinary Office Zurich.

METHOD DETAILS

In vivo treatments and EAE induction

Anti-CSF1R (clone AFS98) was administered by intraperitoneal (i.p.) injection on day 0 (2 mg) and day 2 (1 mg), diluted in PBS, and mice were euthanized on day 9. A 10 μg dose of Flt3L was administered i.p. daily for 9 days, after which mice were euthanized. Tamoxifen (Sigma) was dissolved in ethanol and corn oil to 25 mg/ml and administered in 200 μL doses via oral gavage (5 mg/dose) to *Cx3cr1*^{CreER} *Rosa26*-RFP mice every second day for 8-10 days. After 5 weeks mice were either euthanized or immunized for EAE induction: *Cx3cr1*^{CreER} *Rosa26*-RFP mice (5 weeks after tamoxifen administration) or C57BL/6 mice (aged 8 weeks) were injected with MOG_{35-55} peptide emulsified in Complete Freund's Adjuvant sub-cutaneously (s.c.) and Pertussis toxin i.p., and scored, as previously described (Mrdjen et al., 2017). Peak of disease was defined when mice reached a score of 3-4 at approximately 14 days after immunization.

Tissue harvesting and cell preparation

Mice were sacrificed by injection of pentobarbital (50 μL at 300 mg/ml) i.p. and transcardiac perfusion was performed with PBS and heparin (5 u/ml). The CNS was harvested and the dura mater was removed from the skull and included in the sample. The complete CNS samples (including meninges and choroid plexus) were processed into single cells as previously described (Mrdjen et al., 2017): briefly, the CNS was cut into small pieces in an eppendorf tube and incubated with digestion buffer (RPMI supplemented with 2% FBS, 2 mM HEPES, 0.4 mg/ml Collagenase D and 2 mg/ml DNase) for 30 minutes at 37°C, shaking. Enzymatic digestion was stopped with EDTA (5 mM), the sample was homogenized with a syringe and the homogenate was filtered through a 70 μm cell strainer. This was followed by gradient centrifugation with 30% Percoll (GE Healthcare Life Sciences) in PBS (v/v) (23'500 x *g* for 30 minutes at 4°C without brakes), removal of myelin with a suction pump and filtration to generate a single-cell suspension. The samples were then ready for staining with mass- or fluorescence cytometry antibodies.

Mass cytometry

Mass cytometry antibodies were either labeled in-house using antibody-labeling kits and protocols purchased from Fluidigm. Antibodies were individually titrated and optimized as into the final panel prior to use, ensuring that each parameter was informative. We used 5 palladium metal isotopes for live cell barcoding of samples with CD45 (Mei et al., 2015), while keeping CD45-147Sm as a common channel to clearly identify cells expressing varying degrees of CD45, such as microglia, as previously described (Mrdjen et al., 2017). Briefly, individual samples from steady-state adult, steady-state geriatric and peak EAE adult C57BL/6 mice were incubated with respective CD45-Pd + CD45-147 Sm antibodies in PBS for 30 minutes at 37°C after which they were washed twice with FACS buffer (PBS supplemented with 0.5% BSA), then combined into composite samples. In another experiment, the forebrain and hindbrain were taken from 4-month-old APP/PS1 or littermate control mice, barcoded separately, and combined into composite samples. We used one barcoding CD45-Pd per group in combination with CD45-147 Sm in order to avoid epitope saturation and maintain signal intensity, and were therefore able to barcode 5 samples from separate groups per composite sample. This was followed by incubation of the composite samples with the cocktail of primary panel antibodies (Table S1) for 30 minutes at 37°C, washing with FACS buffer and then incubating with secondary antibodies for 20 minutes at 4°C. After washing, samples were incubated with intercalating solution (Iridium (Sigma) in MaxPar Fix/Perm buffer (Fluidigm)) overnight at 4°C. Prior to acquisition, the samples were washed twice with FACS buffer and once with MilliQ water. Barcoded composite samples were acquired on a Helios mass cytometer (Fluidigm). Quality control and tuning processes on the Helios were performed on a daily basis before acquisition. Data from different days and across acquisition time was normalized by adding five-element beads to the sample immediately before acquisition and using the MATLAB-based normalization software, as described previously (Finck et al., 2013).

Fluorescence cytometry

Samples were incubated with primary antibodies in PBS for 30 min at 4°C, washed with PBS and incubated with secondary antibodies for 20 min at 4°C. After washing, cells were fixed and permeabilized with 100 μL BD Cytofix/Cytoperm™ (containing 4.2% Formaldehyde) for 20 min at 4°C, and washed with Perm buffer (PBS with 0.1% saponin) before intracellular labeling which was performed for CD3, CD4 and CD8 in Perm buffer for 30 min at 4°C, with final washing in Perm buffer. Samples were resuspended in PBS and analyzed by flow cytometry with a FACSymphony™ cell analyzer. Before acquisition, PMT voltages were adjusted manually in order to reduce fluorescence spillover, and single-stain controls were acquired for compensation matrix calculation.

Tracking intra-vascular cells in the CNS

In order to label intra-vascular cells within the steady state CNS we injected PE conjugated anti-CD45 (7.5 μg in PBS) i.v. into adult C57BL/6 mice and euthanized them after 3 minutes, performed transcardiac perfusion and harvested the CNS, as previously described (Anderson et al., 2014). Single cell suspensions were then stained with fluorescence cytometry antibodies.

Immunohistochemistry for BAMs

C57BL/6 mice were transcardially perfused with PBS and heparin (5u/ml) followed by 2%–4% (wt/vol) paraformaldehyde (PFA) in 0.1 M phosphate buffer (pH 7.4). The CNS, excluding the dura mater, was further fixed for 6-12 hours at 4°C and rinsed with PBS followed by cryoprotection with 30% (wt/vol) sucrose in PBS. Samples were embedded in OCT (Medite). Cryo-sectioning was performed with a thickness of 12-30μm using a Hyrax C60 cryostat (Zeiss). The dura mater was fixed for 2-4 hours at 4°C followed by removal from the skull, direct placing onto superfrost plus slides (Thermo Scientific) and storage at −20°C. For quantification of BAM, subsets the choroid plexus was removed from the CNS after fixation and also directly placed onto slides. CNS tissue sections, dura mater and choroid plexus mounts were permeabilized by incubation in blocking solution (PBS supplemented with 0.2% Triton X-100 and 5% normal goat serum) for 1 hour at room temperature. Sections and tissues on slides were labeled primary antibodies either at 4°C, over night or at room temperature for 2 hours, and free-floating sections for 24-72 hours at 4°C in staining solution (PBS supplemented with 0.1% Triton X-100 and 2% normal goat serum): anti-Iba1 (1:500), anti-MHCII (1:200), anti-Lyve1 (1:200), anti-CD206 (1:100) and anti-CD11c (1:40). After washing, samples were incubated either at 4°C overnight or for 1-2 hours at room temperature with the respective secondary antibodies (anti-rabbit, anti-rat, streptavidin, etc., 1:500-700). Washing was repeated and sections were mounted with 1 drop of IS mounting medium with DAPI (Dianova) or SlowFade Gold antifade reagent with DAPI (Invitrogen). Fluorescence photomicrographs were acquired on a Vectra3 (Perkin Elmer) fluorescence microscope using a x20 objective lens. Filters for AF488, AF546, AF647, AF 660 and DAPI were used for imaging tissues to facilitate subsequent unmixing of all colors according to their respective spectra.

Immunohistochemistry for neutrophils

Mice were transcardially perfused using 4% (wt/vol) PFA. The fur was removed and heads (including the skull and brain) were transferred into USEDECALC solution for 6 days (MEDITE Cancer Diagnostics, USA) and decalcified using ultrasonic decalcifying automate USE 33 (Medite® GmbH, Switzerland). Specimens were subsequently sectioned into 3 μm slices and embedded in paraffin for further histological processing. Antigen retrieval was performed on sections by microwave heating at 98°C for 15 min (microMED T/T Mega, Hacker-Milestone) in citrate buffer (0.01M citric acid, pH6).

For brightfield immunostaining, endogenous peroxidases were neutralized by incubation in PBS supplemented with 3% H_2O_2, and non-specific binding blocked using PBS supplemented with 10% FCS. Tissue sections were incubated with unconjugated anti-Ly6G (1:1000). Bound primary antibody was visualized with biotin-labeled anti–rat antibody and streptavidin-peroxidase staining method using polymerized 3,3′-diaminobenzidine (all reagents from Dako; Haemalaun counterstaining of nuclei).

For immunofluorescence staining, non-specific binding was also blocked using PBS supplemented with 10% FCS. Sections were subsequently incubated with unconjugated anti-Ly6G (1:500) and with rabbit anti-vWF antibody (1:1000). Bound antibodies were visualized with AF555–labeled donkey anti–rabbit (1:200) and Cy3-labeled goat anti–rat (1:200) secondary antibodies. Nuclei were stained with DAPI (1:5000). All antibodies were diluted in DAKO Real™ Antibody Diluent.

QUANTIFICATION AND STATISTICAL ANALYSIS

Pre-processing of mass and flow cytometry data

For mass cytometry data live cells were exported by manual gating on Event_length, DNA (191Ir and 193Ir), and live cells (195Pt) using FlowJo software (Tree Star), as previously described (Mrdjen et al., 2017). Next, cells were assigned to their initial samples using Boolean gating in FlowJo. Background subtracted.fcs files were exported from FlowJo, imported into the R environment and transformed using an inverse hyperbolic sine (arcsinh) function with a cofactor of 5 (Bendall et al., 2011). For flow cytometry data, after compensation correction in FlowJo, live, single, background subtracted and compensated cells were exported by manual gating. Samples were not barcoded so debarcoding was not necessary. The appropriate transformation cofactors were determined by uploading the files into Cytobank (https://www.cytobank.org) (Kotecha et al., 2010) and using the Scales feature; thereafter transformation was carried out in MATLAB and transformed files were imported into the R environment for further pre-processing and analysis. To equalize the contribution of each marker in subsequent automated data analysis steps of mass and flow cytometry data, we performed percentile normalization (Levine et al., 2015), normalizing all data to the 99.9^{th} – 99.99^{th} percentile of the merged sample in each experiment, depending on the number of outliers present. This preserves inter-sample variability in maximum expression values, which might be biologically relevant, and normalizes inter-marker maximum expression values, while maintaining original staining indices.

Automated population identification in high-dimensional data analysis

Pre-processing of the raw data was followed by dimensionality reduction and visualization by t-Distributed Stochastic Neighbor Embedding (t-SNE) (Mair et al., 2016; Van Der Maaten and Hinton, 2008) with parameters as listed in the figure legends, clustering with FlowSOM into initial 100 nodes (Van Gassen et al., 2015), followed by expert-guided manual metaclustering using the t-SNE with

overlaid marker expression values and a heatmap of median expression values of the initial automated 100 FlowSOM nodes (Hartmann et al., 2016). In some cases, major cell populations were separated for further clustering into subsets. When comparing different groups, for example steady state and EAE samples, the t-SNE and clustering analyses were performed on the combined datasets. Force- and landmark- directed maps were generated with a modified version of the Scaffold application (Spitzer et al., 2015), and landmark populations that were manually gated in FlowJo and exported. We used the 100 initial FlowSOM nodes as unsupervised Scaffold clusters instead of the built-in clustering algorithm of the Scaffold application. This allowed the validation of expert-guided manual metaclustering by the grouping of FlowSOM nodes around manually-gated landmark nodes in the Scaffold map. Categorical ONE-Sense analysis was performed in the R environment by generating a one-dimensional t-SNE axis using lineage or activation markers, and a progressive lineage or activation heatmap along each axis, which were then arranged side-by-side. Statistics were calculated using Student's t test and the Benjamini-Hochberg post-test for false discovery rates (FDR). Stars were assigned according to the FDR: * = significant (i.e., p value < 0.05) with a FDR of 10%, ** = significant with a FDR of 5% and *** = significant with a FDR of 1%. The *n* number indicates the number of mice used in each experiment.

Quantification of cells from immunohistochemistry

Semi-automated cell detection and quantification of BAM subsets was performed using the implemented Inform Software (Perkin Elmer). A minimum of 5 sections per compartment (dura mater, pia mater, perivascular space, choroid plexus), per mouse were analyzed and a minimum of 4 regions of interest per section. Images used for analyses were taken on the SP8 upright (Leica) with a 20 × emulsion objective at 1024 × 1024 pixels in *xy*. A pinhole size of 60 μm was used. Images were taken in frames with a line average of 16. DAPI and AF546 were detected in one sequence and AF488 and AF647 were detected in a second sequence. Alternatively, images were taken sequentially with a SP5 Leica confocal laser scanning microscope (Leica) equipped with argon and helium lasers and the 40 × (oil immersion, NA1.25) objective. Images were processed and merged by Imaris Imaging software (Bitplane).

DATA AND SOFTWARE AVAILABILITY

Mass cytometry data of CNS leukocytes from C57BL/6 adult, geriatric and EAE mice (https://community.cytobank.org/cytobank/experiments/69323) as well as from 4-month-old APP/PS1 and littermate control mice (https://community.cytobank.org/cytobank/experiments/69324) are available online.